

HypeR Adaptivity: Joint hr -Adaptive Meshing via Hypergraph Multi-Agent Deep Reinforcement Learning

Niccolò Grillo¹, James Rowbottom², Pietro Liò¹, Carola-Bibiane Schönlieb², Stefania Fresca³

¹Department of Computer Science and Technology, University of Cambridge, UK

²Department of Applied Mathematics and Theoretical Physics, University of Cambridge, UK

³Department of Mechanical Engineering, University of Washington, Seattle, WA, USA

Abstract

Adaptive mesh refinement is central to the efficient solution of partial differential equations (PDEs) by means of the finite element method (FEM). Classical r -adaptivity optimizes vertex positions but requires solving expensive auxiliary PDEs such as the Monge-Ampère equation, while classical h -adaptivity modifies topology through element subdivision but suffers from computationally expensive error indicator computation and remains fundamentally constrained by isotropic refinement patterns that impose accuracy ceilings. Combined hr -adaptive techniques naturally outperform single-modality approaches, yet inherit both computational bottlenecks and the restricted cost-accuracy trade-off. An emerging field of machine learning methods for adaptive mesh refinement has sought to overcome these limitations, but existing approaches address h -adaptivity or r -adaptivity in isolation. In this respect, we present HypeR, a deep reinforcement learning framework that jointly optimizes mesh relocation and refinement in a unified formulation. HypeR casts the joint adaptation problem using tools from hypergraph neural networks and multi-agent reinforcement learning. Refinement is formulated as a heterogeneous multi-agent Markov decision process (MDP) where a swarm of element agents decide discrete refinement actions, while relocation follows an anisotropic diffusion-based policy operating on vertex agents with provable prevention of mesh tangling. The reward function combines local and global error reduction to promote general accuracy. Across benchmark PDEs, HypeR reduces approximation error by up to 6–10 \times versus state-of-art h -adaptive baselines at comparable element counts, breaking through the uniform refinement accuracy ceiling that constrains subdivision-only methods. The framework produces meshes with improved shape metrics and alignment to solution anisotropy, demonstrating that jointly learned hr -adaptivity strategies can substantially enhance the capabilities of automated mesh generation.

Keywords: Scientific machine learning, Adaptive mesh refinement, Numerical simulations, Neural networks, Deep Reinforcement Learning

1 Introduction

Partial differential equations (PDEs) model a vast array of physical phenomena, from fluid dynamics and heat transfer to structural mechanics and electromagnetic fields Evans (2010); LeVeque (2007). The finite element method (FEM) has emerged as the predominant numerical method for solving PDEs at scale, offering robustness, well-established error bounds, and mature software implementations Brenner and Scott (2008); Ern and Guermond (2004). However, even with highly optimized solvers, the computational cost of simulations grows rapidly with the number of degrees of freedom (DOFs). Denoting by N the total number of DOFs, memory requirements typically grow superlinearly, and the cost of direct sparse factorization scales as $\mathcal{O}(N^{3/2})$ in two dimensions and as $\mathcal{O}(N^2)$ in three dimensions. By contrast, optimal multigrid or multilevel iterative methods can in many cases achieve $\mathcal{O}(N)$ complexity Saad (2003). This makes large-scale problems computationally prohibitive Babuška and Suri (1994), motivating mesh adaptation: strategically redistributing mesh resolution

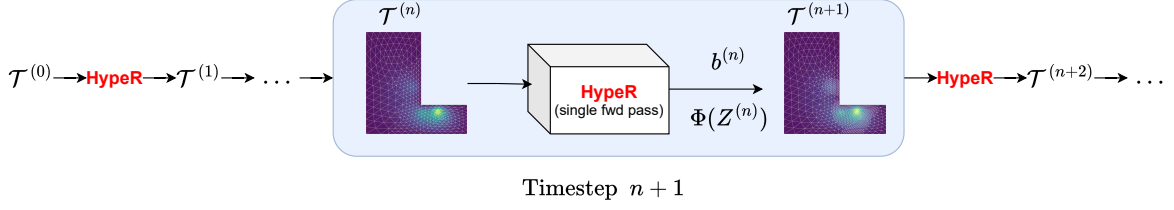


Figure 1: A high-level schematic of the HyperR framework at inference. Starting from an initial coarse mesh $\mathcal{T}^{(0)}$, the HyperR policy network is applied iteratively. At each step, the network takes the current mesh $\mathcal{T}^{(n)}$ and, in a single forward pass, jointly outputs the refinement vector $b^{(n)}$ and the vertex relocation map $\Phi(\mathcal{Z}^{(n)})$ to produce the next adapted mesh $\mathcal{T}^{(n+1)}$.

(i.e., the local density of DOFs or mesh vertices) that optimizes the cost-accuracy trade-off in order to capture solution features where they matter most.

Classical mesh adaptation strategies include two complementary techniques, each addressing different aspects of the accuracy-efficiency trade-off. h -adaptation modifies mesh topology through element subdivision or coarsening, dynamically adjusting local resolution based on a posteriori error estimators. Popular approaches include the Zienkiewicz-Zhu (ZZ) superconvergent patch recovery technique Zienkiewicz and Zhu (1992), which estimates element-wise errors η_K through gradient reconstruction, and Dörfler marking strategies Dörfler (1996), which refine elements contributing to a fixed fraction of the total error Verfürth (1996); Ainsworth and Oden (2000). In contrast, r -adaptation relocates a fixed number of mesh vertices while preserving connectivity, optimizing vertices positions through a continuous mapping Φ . This typically requires solving auxiliary PDE problems, such as the Monge-Ampère equation for optimal transport-based mesh movement Budd et al. (2009); Delzanno et al. (2008); Huang and Russell (2011). While h -methods can arbitrarily increase resolution, they suffer from exponential growth in DOFs. In contrast, r -methods maintain a fixed number of DOFs, but are limited by the initial mesh topology. The optimal strategy - hr -adaptation - combines both approaches, yet traditional numerical methods treat them sequentially, missing potential synergies and requiring complex bookkeeping of element hierarchies and projection operators Alauzet and Loseille (2016); Bank and Xu (2003). Crucially, these combined techniques inherit the computational bottlenecks of both modalities, from solving expensive auxiliary PDEs to costly error indicator computations, limiting their practical efficiency.

An emerging field of machine learning methods has sought to overcome these computational bottlenecks, but existing approaches have largely addressed h -adaptivity or r -adaptivity in isolation. For h -adaptation, deep reinforcement learning (RL) offers a fundamentally different paradigm. By formulating mesh adaptation as a Markov Decision Process (MDP) with state space \mathcal{S} (mesh configurations), action space \mathcal{A} (adaptation operations), and reward function R (error reduction), RL agents can learn policies $\pi : \mathcal{S} \rightarrow \mathcal{A}$ that optimize long-term error-efficiency trade-offs Sutton and Barto (2018) (see Appendix C for detailed RL foundations). This approach has shown promise, with methods like ASMR++ Freymuth et al. (2024a) employing swarm-based multi-agent RL to achieve order of magnitude speedups over uniform refinement. In parallel, graph neural network (GNN) approaches have targeted r -adaptation. Many of these, such as the M2N Song et al. (2022) and UM2N Zhang et al. (2024) families, are trained in a supervised manner to imitate the complex mappings generated by classical auxiliary PDE solvers. A distinct GNN-based strategy, employed by G-Adaptivity Rowbottom et al. (2025), bypasses these expensive targets and instead learns to directly minimize FEM error through differentiable simulation. However, each of these methods addresses only one aspect of mesh adaptation, inheriting fundamental limitations: h -only methods cannot exceed uniform refinement accuracy on the initial topology, while r -only methods cannot add DOFs for emerging features.

In this work, we present HypeR, a deep RL framework that computes relocation and refinement actions in a single forward pass of a hypergraph neural network based rollout strategy. This process, visualized in Figure 1, is applied iteratively starting from a coarse mesh. In each adaptation step, the policy network jointly determines the relocation map Φ through continuous vertex actions and the refinement vector b through discrete element actions. This unified formulation directly optimizes the coupled pair (Φ, b) without resorting to staged procedures where intermediate calculations of the solution are needed, allowing relocation and refinement to inform one another within the same decision process.

HypeR is based on three interconnected principles. First, we represent the mesh as a hypergraph $\mathcal{H}^{(n)} = (\mathcal{Z}^{(n)}, \{K_j^{(n)}\}_j, H^{(n)}, A^{(n)})$, where vertices and element embeddings, i.e., $\mathcal{Z}^{(n)}$ and $\{K_j^{(n)}\}_j$, are linked via incidence and adjacency operators. In particular, hypergraph message passing Yadati et al. (2019) enables bidirectional exchange between the hyper-edges, which represent mesh elements, where agents make decisions of mesh refinement that changes local mesh topology, and vertices where agents make geometric decisions via the movement of each node. As excessive movement incurs a small cost but can strongly impact mesh quality and excessive refinement negates the need for mesh movement at a high computational cost, the coupling ensures that refinement decisions depend on local mesh quality and that relocation anticipates forthcoming subdivisions. Second, we formulate adaptation as a heterogeneous multi-agent Markov Decision Process (MDP) following the swarm RL paradigm Šošić et al. (2017); Hüttenrauch et al. (2019): vertex agents parameterize continuous displacements sampled from Gaussian policies, while element agents sample discrete refinement flags from Bernoulli policies. Third, we guarantee non-tangling relocation: the vertex policy is parameterized through a diffusion-based operator that preserves element orientation by ensuring $\det(J_\Phi|_K) > 0$, for all elements K . This construction prevents inversion while remaining differentiable, providing the orientation-preserving property required for valid FEM computations.

The synergy between the different components enables HypeR to overcome the limitations of existing approaches. More precisely, the hypergraph representation allows element agents to communicate refinement demands to vertex agents, which can relocate in advance vertices so that new elements are well-conditioned before subdivision. Conversely, regions of geometric distortion detected by vertex agents can trigger topological updates, guiding refinement where relocation alone is insufficient. This bidirectional coordination is learned through multi-objective Proximal Policy Optimization (PPO) Schulman et al. (2017) with separate policy and value heads for each agent type, producing meshes unattainable by pure h -adaptive or r -adaptive methods. Beyond error reduction, HypeR demonstrably improves mesh quality: elements exhibit less acute minimum angles, reduced skewness, and smoother gradation. In this way, the resulting anisotropy better aligns element orientation with solution features. These properties, quantified through standard shape metrics, directly enhance stability and approximation accuracy by reducing stiffness matrix conditioning issues and capturing directional features of the PDE solutions. Across benchmark PDEs including Poisson, heat diffusion, Stokes flow, and linear elasticity, HypeR reduces approximation error by up to $6 - 10\times$ compared to state-of-art h -adaptive methods at comparable element counts. Furthermore, the learned policies demonstrate robust zero-shot generalization, successfully adapting to unseen domain geometries and scales significantly larger than those seen during training. This establishes joint reinforcement-learned hr -adaptivity as a unified paradigm for automated mesh generation, achieving lower error and demonstrably higher mesh quality, as measured by classical shape metrics, and alignment with solution fields.

In this study, we validate the HypeR framework primarily on two-dimensional stationary problems using meshes with linear basis functions. However, the underlying formulation—specifically the hypergraph representation and multi-agent reinforcement learning architecture—is inherently dimension-agnostic. As we discuss in the methodology, extending HypeR to three-dimensional domains or higher-order elements requires little to no structural adjustment to the learning algorithm.

1.1 Related Works

In this section we present and review related research ranging from traditional mesh adaptation techniques to most recent machine learning-based methods. Classical methods provide rigorous foundations for h -adaptivity through a posteriori error estimators and marking strategies, and for r -adaptivity through PDE-based and variational relocation schemes. Most recently, learning-based methods framing refinement as a RL problem, relocation as a neural mesh movement task, or mesh generation as a supervised prediction problem, have emerged. These complementary directions, detailed below, define the current landscape, yet none provide a unified learning framework for hr -adaptivity, which is the focus of HypeR.

Traditional mesh adaptation methods. Classical mesh adaptation separates h -methods (element refinement inducing topology modification) from r -methods (vertex relocation entailing geometry modification). Zienkiewicz-Zhu error estimators Zienkiewicz and Zhu (1992) and Dörfler marking Dörfler (1996) represent h -adaptivity foundations with proven convergence rates Binev et al. (2004); Stevenson (2008). In contrast, r -adaptivity relies on different numerical schemes to reposition a fixed set of vertices, such as solving auxiliary PDEs (e.g., the Monge-Ampère equation Budd et al. (2009); Delzanno et al. (2008); Huang and Russell (2011)), optimizing mesh quality via metric-based methods Yano and Darmofal (2012), or minimizing a cost functional through variational approaches McRae et al. (2018). Combined hr -adaptivity strategies exist primarily in specialized applications Nagarajan and Soghrati (2018) using heuristic coordination. These methods rely on hand-crafted rules, limiting their ability to optimize the accuracy-cost trade-offs in complex scenarios.

Reinforcement learning for h -adaptivity. Recent advances in RL have addressed adaptive mesh refinement through various sequential decision-making approaches. Freymuth et al. (2023) introduced swarm-based multi-agent RL (ASMR) where mesh elements act as collaborating agents that can split and therefore increase local mesh density, achieving 2 orders of magnitude speedup over uniform refinement. Its extension ASMR++ Freymuth et al. (2024b) improves upon the previous approach with local rewards based on maximum error reduction, normalized agent mapping for stable reward propagation, and adaptive element penalties enabling multi-resolution policies without retraining. These features enable to overcome fundamental limitations in earlier RL approaches: VDBG Yang et al. (2023b) used value decomposition networks for credit assignment but struggled with training stability on larger meshes, single-agent methods Yang et al. (2023a) suffered from prohibitive inference runtime by refining one element per timestep, and sweep-based approaches Foucart et al. (2023) created training-inference misalignment through random sequential sampling during training versus parallel execution during inference. DDynAMO Dzanic et al. (2024) extends key ideas from multi-agent RL-based h -adaptive mesh refinement to time-dependent problems through anticipatory refinement, but remains constrained by its reliance on structured 2D meshes, fixed observation windows, and PDE-specific features, limiting its scalability and general applicability. Other specialized approaches target specific domains like GMR-Net Kim et al. (2023) for elliptic PDEs, Flow2Mesh Yu et al. (2024) for fluid dynamics, and recurrent networks Bohn and Feischl (2021) for marking strategies. Despite impressive results, all these h -adaptive methods are fundamentally limited to uniform refinement on the initial mesh structure.

Neural approaches to r -adaptivity. Recent approaches for mesh movement have investigated the use of GNNs to overcome the bottleneck of classical velocity-based methods relying on the costly solution of the Monge-Ampère equation. They all employ graph learning-based algorithms to relocate mesh vertices while maintaining fixed connectivity. In this regard, a series of mesh movement networks from the M2N family represent progressive extensions. In particular, M2N Song et al. (2022) introduced end-to-end mesh movement with neural splines and Graph Attention Networks trained on pre-generated Monge-Ampère meshes. UM2N Zhang et al. (2024) enabled zero-shot generalization across PDE types, relying only on the provision of a suitable monitor function and using graph transformer encoders, and UGM2N Wang et al. (2024) eliminated the dependency on pre-adapted meshes through unsupervised learning with localized geometric features. Rowbottom

et al. (2025) proposed G-Adaptivity: a GNN diffusion-based vertex relocation framework which directly minimizes FEM error, through differentiable FEM solving, and preserves mesh validity via the diffusion-based formulation. Moreover, recent works include data-free approaches Hu et al. (2024) and alternative diffusion-based frameworks Yu et al. (2025). All these approaches achieve 10-100 \times speedups over classical methods, however, these r -adaptive methods operate only on fixed connectivity, preventing resolution enhancement through refinement, which represents a fundamental limitation for evolving features or singularities.

Supervised learning for mesh generation. Adaptive meshing by expert reconstruction (AMBER) Freymuth et al. (2025) introduced a multi-scale hierarchical GNN trained with an experience replay buffer to predict the sizing field extracted from human expert generated meshes. The sizing field is then injected into standard full mesh generation algorithms for use in downstream tasks. GraphMesh Khan et al. (2024) utilises a GCN based architecture to predict error distributions on meshes for general polygonal domains utilising domain aware nodes features in the form of mean value coordinates, while earlier works, like MeshingNet Zhang et al. (2020) and its 3D extension Zhang et al. (2021), learn from a posteriori error estimate. Finally, image-based methods Huang et al. (2021) using CNNs on discretized domains struggle with varying resolution requirements. These supervised approaches require expert data or specific error estimates, limiting their generalization and applicability compared to RL methods.

1.2 Main Contributions

This work introduces HypeR, the first RL framework for unified hr -adaptivity. Our main contributions are:

- **Joint hr -adaptive RL formulation.** We present a framework that learns simultaneous mesh relocation and refinement policies through a dual-swarm MDP. Unlike prior works, restricted to either h -adaptivity (ASMR++, VDBG) or r -adaptivity (M2N, UM2N, G-Adaptivity), our approach discovers coordinated strategies that exploit the synergy between topology and geometry modifications.
- **Hypergraph neural architecture with heterogeneous message passing.** We introduce a novel mesh representation that treats vertices and elements as distinct node types in a hypergraph, enabling specialized information flow between geometric and topological levels. This architecture captures this duality in mesh adaptation, through separate but coupled embedding spaces connected by hypergraph convolutions.
- **Provably valid mesh operations through diffusion-based relocation.** We integrate the diffusion-based movement guarantees from G-Adaptivity into a learned policy framework, ensuring mesh validity. This bridges the gap between classical numerical guarantees and modern deep learning, providing the first RL approach to r -adaptivity that provably prevents mesh tangling, including non-convex domains.
- **Multi-objective optimization with distinct agent rewards.** We formulate mesh adaptation as a heterogeneous multi-agent problem where vertex and element agents optimize different objectives on different timescales. Vertex agents use short-horizon rewards ($\gamma_r \ll 1$) for immediate error reduction through relocation, while element agents employ long-horizon returns ($\gamma_h \approx 1$) to capture the forward impact of refinement decisions. Thanks to the differentiability of the RL loss, simultaneous gradient-based optimization of both refinement and relocation is possible.
- **Curriculum learning for coupled policy optimization.** We develop a two-phase training curriculum that addresses the non-stationary learning dynamics of joint adaptation. By initially training relocation with random refinement before enabling coordinated learning, we stabilize convergence and obtain robust policies that generalize to different PDE parameters and domain shapes and sizes.
- **Enhancement in adaptive mesh refinement accuracy.** HypeR achieves 6–10 \times error reduction compared to state-of-art h -adaptive methods at equivalent element counts across four benchmark PDEs. By

overcoming the uniform refinement approximation limit, a fundamental barrier for all existing h -only methods, we demonstrate that joint hr -adaptation demonstrates the ability of an order of magnitude improvement over single adaptivity based methods.

These contributions establish that treating mesh adaptation as a unified optimization problem, rather than sequential h - and r -steps, could open up new possibilities of what is achievable in automated mesh generation.

2 Mathematical Framework

This section establishes the mathematical setting for our work. We begin by introducing the abstract stationary PDE problem and its FEM discretization. Then, we provide formal definitions for mesh relocation (r -adaptivity) and mesh refinement (h -adaptivity), framing them as two distinct optimization problems. Finally, we outline the conventional iterative process that combines these two techniques, setting the stage for the unified approach proposed in this paper.

2.1 PDE Setting

Let $\Omega \subset \mathbb{R}^d$ (with $d = 2$) be a bounded domain, which we refer to as the physical domain. Within this work, we consider PDEs parametrized by a set of parameters, namely $\boldsymbol{\mu} \in \mathcal{P} \subset \mathbb{R}^p$, with \mathcal{P} compact:

$$\begin{cases} \mathcal{N}[\boldsymbol{\mu}](u) = 0 & \text{in } \Omega, \\ \mathcal{B}[\boldsymbol{\mu}](u) = 0 & \text{on } \partial\Omega, \end{cases}$$

where \mathcal{N} is a generic nonlinear differential operator and \mathcal{B} enforces the boundary conditions. To solve problem (2.1) numerically, we introduce a triangulation \mathcal{T} of the computational domain and define $\tilde{\Omega} = \text{int}(\bigcup_{K \in \mathcal{T}} K)$, with $\tilde{\Omega} \approx \Omega$. On the mesh \mathcal{T} , we consider a finite-dimensional Galerkin space X_h of dimension $\dim(X_h) = N_h$; here, by h we denote a parameter related to the mesh size of the computational grid.

By applying the Galerkin-FEM on X_h , the discretized problem reads as follows:

$$\mathbf{N}[\boldsymbol{\mu}](\mathbf{u}) = 0.$$

We remark that the mesh \mathcal{T} is defined by a set of vertices (or nodes) $\mathcal{Z} = \{\mathbf{z}_i\}_{i=1}^{N_v}$, with $N_v = N_h$, and their connectivity matrix \mathcal{C} , which defines the elements $\{K\}_{i=1}^{N_e}$. The goal of mesh adaptivity, or adaptive meshing, is to construct a mesh \mathcal{T} by minimizing a suitable error metric $E_{\mathcal{T}} = E(\{u(\mathbf{z}_i)\}_{i=1}^{N_v}, \mathbf{u})$, taking into account the discretization error measured in a suitable norm. In this setting, posteriori error estimators are often used to guide the adaptive meshing by providing local error indicators $\{\eta_K\}_{K \in \mathcal{T}}$, which approximate the contribution of each element K to the total error.

2.2 r -Adaptivity: Mesh Relocation via Optimal Transport

The goal of r -adaptivity, or mesh relocation, is to adjust the spatial positions of the mesh vertices \mathcal{Z} to improve approximation accuracy, while keeping the number of vertices and the mesh connectivity fixed. This is formally achieved by identifying a mapping from a fixed reference domain to the physical domain.

Let Ω_F be a computational domain (e.g., the unit square) with a fixed, uniform mesh. Mesh relocation is defined by a differentiable and invertible deformation map $\Phi : \Omega_F \rightarrow \tilde{\Omega}$ which transforms the fixed vertex coordinates $\boldsymbol{\xi}_i \in \Omega_F$ to new vertex coordinates $\mathbf{z}_i = \Phi(\boldsymbol{\xi}_i)$ in the domain $\tilde{\Omega}$. The adapted mesh is then \mathcal{T}_{Φ} , formed by the new vertices $\mathcal{Z}_{\Phi} = \{\mathbf{z}_i\}_{i=1}^{N_v} = \{\Phi(\boldsymbol{\xi}_i)\}_{i=1}^{N_v}$ and the original connectivity \mathcal{C} . The main idea to construct an effective map Φ is to rely on the *equidistribution principle* Budd et al. (2009); Huang and Russell (2011). This principle aims at uniformly distributing a scalar monitor function $m : \tilde{\Omega} \rightarrow \mathbb{R}$, such that $m(\mathbf{z}) > 0 \forall \mathbf{z} \in \tilde{\Omega}$, in the computational domain. The monitor function (such as an apriori estimate of the interpolation error, or the curvature of the solution, through the norm of the hessian) is designed to have

large values in regions of the domain where fine mesh resolution, i.e., small elements' size, is needed. The equidistribution principle is expressed as:

$$m(\Phi(\xi)) \det(J_\Phi(\xi)) = \theta,$$

where J_Φ is the Jacobian of the map Φ and θ is a normalization constant defined as $\theta = |\Omega_F|^{-1} \int_{\tilde{\Omega}} m(z) dz$.

However, the equidistribution principle sets the desired mesh density but it does not uniquely define the map Φ in dimensions $d > 1$. To obtain a unique and well-behaved, i.e., non-tangling mesh, this condition is coupled with an optimal transport requirement Budd et al. (2009). More precisely, the map Φ is chosen to minimize the transport cost functional. For the quadratic cost, this corresponds to minimize the squared $L^2(\Omega_F)$ norm of the displacement field $I_2 = \int_{\Omega_F} |\Phi(\xi) - \xi|^2 d\xi$. By Brenier's theorem Brenier (1991), the unique optimal transport map for a quadratic cost is the gradient of a convex scalar potential $\phi : \Omega_F \rightarrow \mathbb{R}$, such that $\Phi = \nabla_\xi \phi$. Substituting this expression into the equidistribution equation yields the fully nonlinear Monge-Ampère equation for the potential ϕ :

$$\det(D^2 \phi(\xi)) = \frac{\theta}{m(\nabla_\xi \phi(\xi))}.$$

Solving this elliptic PDE for ϕ defines the optimal vertex locations Budd et al. (2009). However, solving it directly is computationally expensive and practical alternatives include relaxation methods, like the Parabolic Monge-Ampère (PMA) formulation, and variational mesh energy minimization Delzanno et al. (2008); Huang and Russell (2011).

Ultimately, we note that a r -adaptivity problem can be expressed as an optimization problem where the goal is to find an optimal valid mapping Φ^* minimizing the error:

$$\Phi^* = \arg \min_{\Phi: \text{valid}} E_{\mathcal{T}},$$

where a mapping is considered valid if it is an orientation-preserving diffeomorphism. This physically means that elements do not invert or overlap, which is mathematically guaranteed if the determinant of the map's Jacobian, $\det(J_\Phi)$, remains positive throughout the domain.

2.3 h -Adaptivity: Mesh Refinement as Decision Problem

h -adaptivity, or mesh refinement, aims at modifying the mesh topology by selectively subdividing elements to increase resolution locally. It can be formalized as a discrete decision problem.

Let the current mesh be $\mathcal{T} = (\mathcal{Z}, \mathcal{C})$, where \mathcal{Z} is the set of vertices and \mathcal{C} is the connectivity of the elements. We introduce a binary decision vector $\mathbf{b} = \{b_K\}_{K \in \mathcal{T}} \in \mathbb{R}^{N_e}$, where $b_K \in \{0, 1\}$ such that $b_K = 1$ means element refinement, and $b_K = 0$ no change. Thus, applying the refinement decisions in \mathbf{b} produces a new mesh $\mathcal{T}_b = (\mathcal{Z}_b, \mathcal{C}_b)$. The new element set \mathcal{C}_b consists of the original unmarked elements and the children of the marked elements, while the new vertex set \mathcal{Z}_b includes new vertices created during subdivision. Conformity is maintained by ensuring no hanging nodes, which in 2D is handled by conformity-preserving procedures like red-green-blue refinement that refines adjacent elements as needed Carstensen (2004).

The optimal refinement strategy seeks to balance error reduction with computational cost. This can be formulated as the minimization of an objective functional:

$$\mathcal{J}(\mathbf{b}) = E_{\mathcal{T}_b} + \alpha \text{Cost}(\mathbf{b}),$$

where $\text{Cost}(\mathbf{b})$ is a penalty term for the increase in the number of DOFs, and $\alpha > 0$ is a weighting parameter. The ideal set of refinements, for one iteration, is given by the solution to the combinatorial optimization problem:

$$\mathbf{b}^* = \arg \min_{\mathbf{b} \in \{0,1\}^{N_e}} \mathcal{J}(\mathbf{b}).$$

Classical numerical algorithms, such as those using Dörfler marking Dörfler (1996), approximate the solution of the optimization problem by marking all elements whose local error indicators $\{\eta_K\}_{K \in \mathcal{T}}$ contribute to a fixed fraction of the total error resulting in a short-term and greedy approach. In contrast, a learning-based approach can train a policy π to predict the decision b_K for each element, aiming to directly approximate \mathbf{b}^* by learning the long-term trade-off between error and cost.

2.4 *hr*-Adaptivity

Combining *r*- and *h*-adaptivity results in a *hr*-adaptive strategy, which is typically performed as an iterative loop. In particular, given a mesh $\mathcal{T}^{(n)}$ at iteration n , the process is as follows:

1. Solve: Compute the discrete solution $\mathbf{u}_{\mathcal{T}}^{(n)}$ on the current mesh $\mathcal{T}^{(n)}$.
2. *r*-Step (Relocation): Determine a valid relocation map $\Phi^{(n)}$ based on $\mathbf{u}_{\mathcal{T}}^{(n)}$ to produce an intermediate moved mesh $\tilde{\mathcal{T}}^{(n)} = \mathcal{T}_{\Phi^{(n)}}$.
3. (Optional) Solve on Moved Mesh: Resolve or estimate the approximation error on $\tilde{\mathcal{T}}^{(n)}$ to obtain updated error indicators for the refinement step.
4. *h*-Step (Refinement): Using error indicators from $\tilde{\mathcal{T}}^{(n)}$ (or $\mathcal{T}^{(n)}$), determine a refinement vector $\mathbf{b}^{(n)}$ to generate the mesh for the next iteration, $\mathcal{T}^{(n+1)} = (\tilde{\mathcal{T}}^{(n)})_{\mathbf{b}^{(n)}}$.
5. Update: Set $n \leftarrow n + 1$ and repeat until a stopping criterion is satisfied (e.g., error tolerance or computational budget).

In a fully unified framework, one could seek to find the pair (Φ, \mathbf{b}) that jointly optimizes a combined objective:

$$\mathcal{J}(\Phi, \mathbf{b}) = E_{\mathcal{T}_{\Phi, \mathbf{b}}} + \alpha \text{Cost}(\mathbf{b}), \quad (1)$$

where $\mathcal{T}_{\Phi, \mathbf{b}}$ is the mesh created by first applying the map Φ and then refining according to \mathbf{b} . Since solving this combined problem is intractable, practical methods decouple the two adaptive steps. However, the decisions can be strongly coupled, for instance, through a shared learned policy that considers both vertex- and element-based features to determine mesh movement and refinement simultaneously. Our proposed work explores precisely this argument by casting the *hr*-adaptivity problem in a deep RL framework, where a joint policy over (Φ, \mathbf{b}) is learned to optimize the long-term error-cost trade-off.

3 Unified Learning Framework for *hr*-Adaptivity

In this section, we introduce *HypeR*, a deep RL framework designed to solve the combined *hr*-adaptivity problem defined in Section 2. *HypeR* learns a single, unified policy that jointly determines the vertex relocation map Φ and the element refinement vector \mathbf{b} in a single iterative loop. This approach is in contrast with classical numerical methods that treat relocation and refinement as separate, sequential steps.

3.1 Mesh Representation as a Hypergraph

Let $\mathcal{T}^{(n)}$ be a conforming mesh of the domain $\tilde{\Omega} \subset \mathbb{R}^d$ at the n -th step of the adaptive mesh refinement process. Here, n indexes the successive iterations of our *hr*-adaptive algorithm, where each iteration involves: (1) solving the PDE on the current mesh, (2) applying the learned relocation policy to move vertices, and (3) applying the learned refinement policy to subdivide selected elements. The mesh is defined by its set of vertices

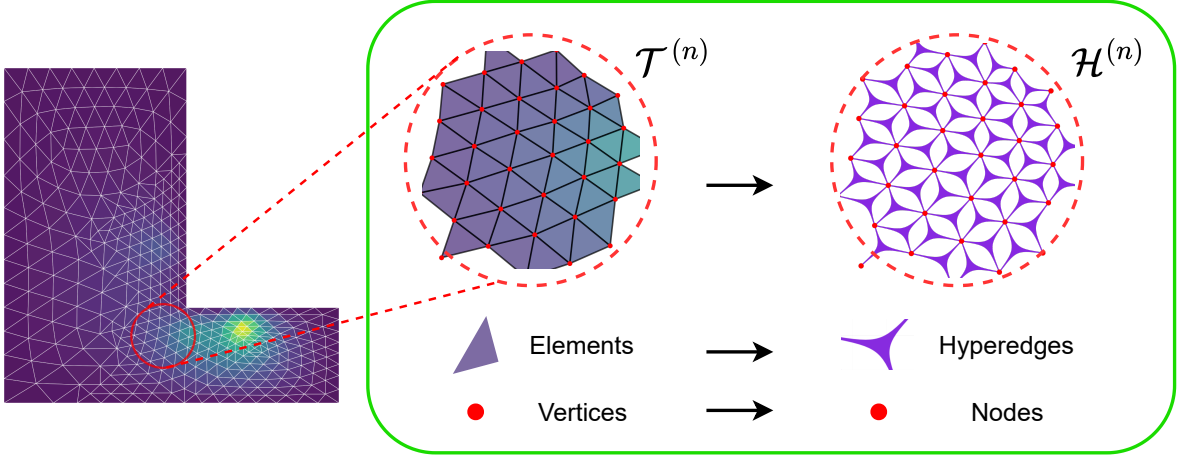


Figure 2: Hypergraph representation of the mesh $\mathcal{T}^{(n)}$. A zoomed-in region of the mesh on the L-shaped domain shows its modeling by the hypergraph $\mathcal{H}^{(n)}$. This encoding creates a one-to-one mapping where each mesh vertex (red dot) is treated as a hypergraph node, and each triangular element is represented as a hypergraph hyperedge (purple) connecting its constituent nodes.

$\mathcal{Z}^{(n)} = \{\mathbf{z}_i^{(n)}\}_{i=1}^{N_v^{(n)}}$ and its set of elements (e.g., triangles or tetrahedra) $\{K_j^{(n)}\}_{j=1}^{N_e^{(n)}}$ ¹. To represent the mesh in a form suitable for processing by GNNs and hypergraph neural networks, we encode $\mathcal{T}^{(n)}$ as a hypergraph $\mathcal{H}^{(n)}$, as illustrated in Figure 2. This encoding creates a one-to-one mapping where each mesh vertex becomes a hypergraph node and each mesh element a hyperedge connecting its defining nodes. Formally, this structure is defined as:

$$\mathcal{H}^{(n)} = (\mathcal{Z}^{(n)}, \{K_j^{(n)}\}_j, H^{(n)}, A^{(n)}),$$

where $H^{(n)} \in \{0, 1\}^{N_v \times N_e}$ is the incidence matrix with $[H^{(n)}]_{ij} = 1$ if vertex $\mathbf{z}_i^{(n)}$ belongs to element $K_j^{(n)}$, and $A^{(n)} \in \{0, 1\}^{N_v \times N_v}$ is the adjacency matrix where $[A^{(n)}]_{ik} = 1$ if vertices $\mathbf{z}_i^{(n)}$ and $\mathbf{z}_k^{(n)}$ share at least one element. These matrices encode the complete mesh topology.

To capture the geometrical features of the mesh and the physical state of the PDE solution, each vertex $\mathbf{z}_i^{(n)}$ and element $K_j^{(n)}$ are augmented with additional features as follows:

$$\mathbf{f}_{\mathbf{z}_i^{(n)}} = [\mathbf{z}_i^{(n)}, \mathbf{u}_i^{(n)}] \in \mathbb{R}^{d_v}, \quad \mathbf{f}_{K_j^{(n)}} = [|K_j^{(n)}|, \text{shape metrics}, \text{solution variability metrics}] \in \mathbb{R}^{d_e}$$

where $\mathbf{u}_i^{(n)}$ is the FEM solution at vertex $\mathbf{z}_i^{(n)}$, and $|K_j^{(n)}|$ is the area (or volume) of element $K_j^{(n)}$. The element shape and solution variability metrics are chosen to quantify mesh quality and local solution behavior, respectively (see Appendix B for more details).

In this way, the hypergraph representation $\mathcal{H}^{(n)}$ provides a unified data structure that encapsulates the mesh topology (via $H^{(n)}, A^{(n)}$), its geometry, including vertex coordinates, element areas and skewness, and the physical solution field (via $\mathbf{f}_{\mathbf{z}_i^{(n)}}, \mathbf{f}_{K_j^{(n)}}$), preparing it for processing by the GNN-based policy network. It is crucial to note that this representation is dynamic: as h -adaptivity subdivides elements, new vertices are created and parent elements are replaced by their children. Consequently, the dimensions of the incidence matrix $H^{(n)}$ and adjacency matrix $A^{(n)}$ must expand, by adding new rows for the vertices and updating the column structure to reflect the new elements. This changing agent population necessitates a formal mechanism to trace lineage and map rewards across steps, a challenge addressed in the following section.

¹The number of vertices $N_v^{(n)}$ and elements $N_e^{(n)}$ change with each adaptation step n . For the sake of clarity, we hereafter omit the superscript (n) from N_v and N_e .

3.2 Adaptive Dual-Swarm Markov Decision Process

We frame the problem of finding an optimal sequence of hr -adapted meshes as a MDP. The objective is to learn a policy π_θ that, given the current mesh, selects a near-optimal pair $(\Phi^{(n)}, \mathbf{b}^{(n)})$ to minimize the long-term, cumulative objective functional \mathcal{J} introduced in Section 2.4 in (1). This is achieved by treating each mesh vertex and element as an independent actor-critic in a swarm of agents. In this paradigm, each agent’s ”actor” component learns a policy to select an action (a vertex move or an element split), while its ”critic” component learns to estimate the long-term value of taking that action from the current state.

Formally, the state at iteration n is the mesh hypergraph $S^{(n)} = \mathcal{H}^{(n)}$. The action $A^{(n)} = (A^{(n),r}, A^{(n),h})$ is a joint decision composed of contributions from the two swarms. The refinement action $A^{(n),h}$ is the binary decision vector $\mathbf{b}^{(n)} = \{a_{K_j}^{(n)}\}_{j=1}^{N_e}$. The relocation action $A^{(n),r}$ is realized through the vertex policy π_θ^r , which learns to approximate the optimal map Φ^* introduced in Section 2.2. At each step n , the vertex policy takes the current state $S^{(n)}$ and outputs a distribution over new coordinates for each vertex. The action for a single vertex, $\mathbf{a}_{\mathbf{z}_i}^{(n)} \in \mathbb{R}^d$, is a sample from this distribution representing its proposed new location. The collective set of actions $A^{(n),r} = \{\mathbf{a}_{\mathbf{z}_i}^{(n)}\}_{i=1}^{N_v}$ thus defines the relocated vertex set $\mathcal{Z}^{(n+1)}$ for the subsequent mesh.

A central challenge in the definition of such an MDP is to keep track of the agent hierarchy as the elements are refined and new vertices are added. To assign credit correctly, we define projection maps that trace an agent’s lineage. For an element $K_j^{(n)}$ at iteration time n , we use a map $\phi_{n \rightarrow n+k}^h(j, j')$ that traces its descendants $\{K_{j'}\}$ at time $n+k$, following the same procedure as in ASMR++ (Freymuth et al., 2024b, Sec. 3.1). However, for vertex agents a similar ”complete” projection is computationally prohibitive. Since h -refinement creates new vertices at each step, a full credit assignment would necessitate a complex, multi-step reward aggregation backward through time. If we consider a 2D triangle refined element, it not only generates 4 new elements but also adds 3 new vertices, shared with neighboring elements. So, a reward received by a new vertex created at step $n+k-1$, realized at $n+k$, would first need to be distributed back to all its parent vertices at $n+k-1$. This aggregation process would then need to be recursively applied for every preceding step $(n+k-2, \dots, n)$ to correctly route all future reward signals back to the original agents. Tracking this dynamic, recursive credit flow for every agent across every trajectory is infeasible in a large-scale learning setting. To overcome this issue, we adopt a practical approximation motivated by the short-term nature of the relocation task. Unlike element refinement, which permanently alters the mesh topology with long-term consequences, vertex relocation (r -adaptivity) is a local tuning of the current geometry whose benefit is realized entirely in the immediate error reduction of the next step. Instead of a full projection, we use a simple identity mapping for vertices:

$$\phi_{n \rightarrow n+k}^r(i, i') = \begin{cases} 1, & \text{if } \mathbf{z}_{i'}^{(n+k)} \text{ and } \mathbf{z}_i^{(n)} \text{ refer to the same persistent vertex,} \\ 0, & \text{otherwise.} \end{cases}$$

This map is ”incomplete” because it only attributes rewards from vertices that persist from iteration n , effectively ignoring the reward contributions from any vertices created in subsequent refinement steps. However, since the primary goal of vertex relocation is immediate, local error reduction, we can pair this simplified map with a very small discount factor $\gamma_r \ll 1$. This enforces a short-term learning objective where the discounted value of future rewards - and thus the error introduced by the incomplete projection - becomes negligible. Therefore, the vertex agents’ discounted long term reward reduces too:

$$G_{\mathbf{z}_i}^{(n),r} = \sum_{k=0}^{\infty} \gamma_r^k \sum_{\mathbf{z}_{i'} \in \mathcal{Z}^{(n+k)}} \phi_{n \rightarrow n+k}^r(i, i') r_{\mathbf{z}_{i'}}^{(n+k),r} \approx r_{\mathbf{z}_i}^{(n),r}.$$

In contrast, the element agents (h -adaptivity) use a large discount factor $\gamma_h \approx 1$ and the full projection map to capture the long-term consequences of refinement:

$$G_{K_j}^{(n),h} = \sum_{k=0}^{\infty} \gamma_h^k \sum_{K_{j'} \in \mathcal{T}^{(n+k)}} \phi_{n \rightarrow n+k}^h(j, j') r_{K_{j'}}^{(n+k),h}.$$

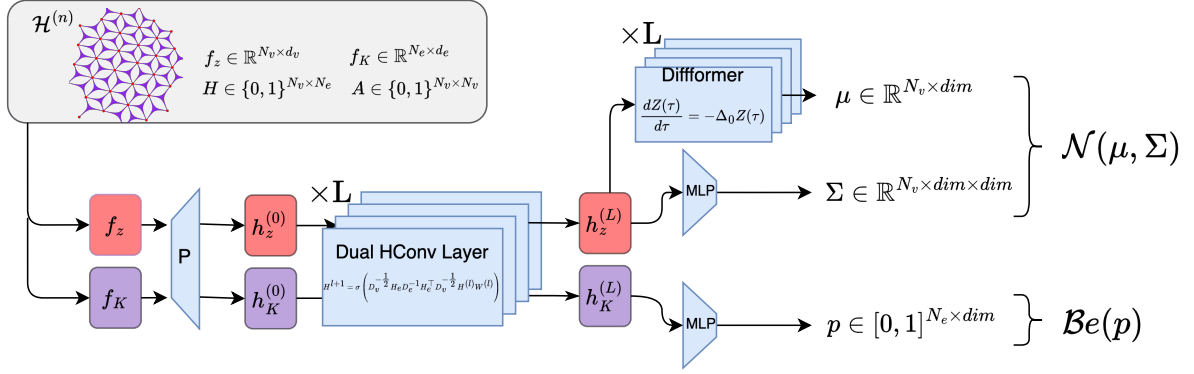


Figure 3: HypeR policy (actor) network architecture. The mesh hypergraph $\mathcal{H}^{(n)}$ provides vertex features (f_z) and element features (f_K), which are first projected onto a latent space by a linear embedding layer (P). The resulting embeddings ($h_z^{(0)}, h_K^{(0)}$) are processed by L dual hypergraph convolutional (HConv) layers to produce the final embeddings $h_z^{(L)}$ and $h_K^{(L)}$. These are fed into two distinct agent policy heads: (1) the vertex-agent head generates a multivariate Gaussian policy $\mathcal{N}(\mu, \Sigma)$ by using a stack of L Diffformer layers to produce the mean μ and a separate MLP to produce the covariance Σ , and (2) the element-agent head uses a MLP to generate a probability vector p for the Bernoulli refinement policy $\mathcal{B}e(p)$. The corresponding value (critic) heads, which share the same hypergraph backbone, are omitted for clarity.

Then, the policy is factorized across the two swarms, assuming conditional independence given the global mesh state $\mathcal{H}^{(n)}$:

$$\pi_\theta(A^{(n)}|S^{(n)}) = \prod_{z_i \in \mathcal{Z}^{(n)}} \pi_\theta^r(a_{z_i}^{(n)}|\mathcal{H}^{(n)}) \times \prod_{K_j \in \mathcal{T}^{(n)}} \pi_\theta^h(a_{K_j}^{(n)}|\mathcal{H}^{(n)}).$$

The policy in (3.2) is optimized via a multi-objective PPO algorithm Schulman et al. (2017) to simultaneously maximize the expected returns $\mathbb{E}[G^r]$ and $\mathbb{E}[G^h]$.

3.3 Neural Network Architecture

The joint policy $\pi_\theta(A^{(n)}|S^{(n)})$ and its associated value functions are parameterized by a single actor-critic neural network. The architecture of the policy (actor) component is illustrated in Figure 3. This network is designed to process the full mesh hypergraph $\mathcal{H}^{(n)}$, leveraging a shared hypergraph-convolutional backbone to extract rich features before feeding them into specialized output heads for each agent swarm (vertices and elements). This architecture allows the network to learn complex dependencies between vertex positions, element shapes, and the local behavior of the PDE solution. The architectural components are detailed below.

Initial feature transformation. The input feature vectors for vertices, $\mathbf{f}_{z_i}^{(n)} \in \mathbb{R}^{d_v}$, and elements, $\mathbf{f}_{K_j}^{(n)} \in \mathbb{R}^{d_e}$, are first projected into a D -dimensional latent space using separate linear transformations. This creates the initial embeddings for the subsequent message passing layers

$$\mathbf{h}_{z_i}^{(0)} = W_v \mathbf{f}_{z_i}^{(n)} \quad \text{and} \quad \mathbf{h}_{K_j}^{(0)} = W_e \mathbf{f}_{K_j}^{(n)},$$

where $W_v \in \mathbb{R}^{D \times d_v}$ and $W_e \in \mathbb{R}^{D \times d_e}$ are learnable weight matrices.

²Throughout this section, we suppress the step superscript $^{(n)}$ from vertex and element notation for readability. All quantities z_i , K_j , and their associated embeddings are implicitly at adaptation step n .

Hypergraph convolutional operations. The core of the neural network consists of L layers of dual hypergraph convolution (HConv) (see Appendix C.5.2 for more details), which enables message passing between vertices and elements. At each layer $\ell \in \{1, \dots, L\}$, embeddings are updated via a two-stage process: *Vertex-to-Element*, where information is passed from vertices to their incident elements to update the element embeddings, and *Element-to-Vertex*, where information is then passed back from the newly updated element embeddings to their incident vertices

$$\tilde{\mathbf{h}}_{K_j}^{(\ell)} = \text{HConv}_{\mathcal{Z} \rightarrow \mathcal{K}}(\{\mathbf{h}_{z_i}^{(\ell-1)}\} \{\mathbf{h}_{K_j}^{(\ell-1)}\}) \quad \text{and} \quad \tilde{\mathbf{h}}_{z_i}^{(\ell)} = \text{HConv}_{\mathcal{K} \rightarrow \mathcal{Z}}(\{\mathbf{h}_{z_i}^{(\ell-1)}\}, \{\tilde{\mathbf{h}}_{K_j}^{(\ell)}\}).$$

Each message passing step is followed by a point-wise nonlinearity (i.e., ReLU) to produce the final embeddings for that layer, $\mathbf{h}_{z_i}^{(\ell)}$ and $\mathbf{h}_{K_j}^{(\ell)}$. After L layers, the final embeddings $\mathbf{h}_{z_i}^{(L)}$ and $\mathbf{h}_{K_j}^{(L)}$ encode contextual information about the L -hop neighborhood of each entity within the mesh.

Output heads. The final embeddings are processed by separate heads for each agent type to produce action distributions and value estimates.

Element agent heads. For each element K_j , its final embedding $\mathbf{h}_{K_j}^{(L)}$ is passed to:

- Policy head: A two-layer MLP, i.e., $\text{MLP}_{\text{elem}}^{\pi}$, that outputs a logit $\ell_{K_j} \in \mathbb{R}$. This logit parameterizes a Bernoulli distribution for the binary refinement action $a_{K_j} \in \{0, 1\}$, which consists of a component of the refinement vector $\mathbf{b}^{(n)}$;
- Value head: A separate two-layer MLP, i.e., $\text{MLP}_{\text{elem}}^V$, that provides as output a scalar value estimate $V_{K_j}^e \in \mathbb{R}$.

Vertex agent heads. For each vertex z_i , its final embedding $\mathbf{h}_{z_i}^{(L)}$ is passed to:

- Policy head: This head determines the parameters defining a multivariate Gaussian distribution over the vertex's new coordinates in \mathbb{R}^d . It consists of two main components. The first one is a *diffformer block*, first introduced in G-Adaptivity Rowbottom et al. (2025), which takes the vertex's current coordinates z_i , together with its embedding $\mathbf{h}_{z_i}^{(L)}$, and provides as output the mean of the distribution $\boldsymbol{\mu}_i \in \mathbb{R}^d$ ³. The second component consists of a separate MLP which produces the covariance matrix $\boldsymbol{\Sigma}_i$. Thus, the policy for the vertex agent is $\pi_{\theta}^r(\cdot | \mathcal{H}^{(n)}) = \mathcal{N}(\boldsymbol{\mu}_i, \boldsymbol{\Sigma}_i)$;
- Value head: A two-layer MLP, i.e., $\text{MLP}_{\text{vert}}^V$, that gives as output a scalar value estimate $V_{z_i}^v \in \mathbb{R}$.

In summary, the overall network is fed with the hypergraph $\mathcal{H}^{(n)}$ and outputs, for each vertex, the parameters of a Gaussian distribution $\mathcal{N}(\boldsymbol{\mu}_i, \boldsymbol{\Sigma}_i)$ to guide relocation, and for each element, a Bernoulli probability to guide refinement. This process directly translates the high-level representation of the state of the mesh to the low-level actions that define the *hr*-adaptation step.

3.3.1 Diffformer Block and Non-Tangling Guarantee

The vertex relocation map $\Phi^{(n)}$ is sampled from the multivariate Gaussian distribution output of the vertex agent policy head. This is built from the *diffformer* operator, a GNN block, first introduced in G-Adaptivity Rowbottom et al. (2025), inspired by classical velocity-based methods and in which vertex relocation is casted as a graph diffusion process. More precisely, the evolution of vertex coordinates $\mathcal{Z}(\tau)$ over a continuous pseudo-time τ is governed by the ordinary differential equation (ODE):

$$\frac{d\mathcal{Z}(\tau)}{d\tau} = (A_{\theta} - I)\mathcal{Z}(\tau) = -\Delta_{\theta}\mathcal{Z}(\tau),$$

³More details on the diffformer block can be found in Section 3.3.1.

initialized with the current mesh coordinates, i.e., $\mathcal{Z}(0) = \mathcal{Z}^{(n)}$. Here, Δ_θ is a learnable, weighted graph Laplacian (details in Appendix E.3). The row-stochastic attention matrix A_θ is computed dynamically from the final vertex embeddings $\{\mathbf{h}_{\mathbf{z}_i}^{(L)}\}_{i=1}^{N_v}$ provided by the shared hypergraph backbone. This allows the diffusion to be anisotropic and data-driven, conditioned on the rich state information captured by the hypergraph.

In practice, this ODE is integrated over a fixed interval using a forward Euler scheme with step size $\delta\tau$. The key result, established in G-Adaptivity Rowbottom et al. (2025), is that the discrete evolution is guaranteed to prevent the critical failure mode of mesh tangling, in which elements become inverted and geometrically invalid. For a sufficiently small step size ($\delta\tau < 0.5$), the transformation matrix $(I - \delta\tau\Delta_\theta)$ has a positive determinant, which ensures that all element orientations are preserved throughout the relocation. Intuitively, the diffusion process moves each vertex into the convex hull of its neighbors, making element inversion impossible.

Within HypeR, the final vertex positions $\mathcal{Z}(T)$ computed by the diffformer serve as the mean $\boldsymbol{\mu}$ for the Gaussian vertex policy. During the training phase, agent actions sampled from the vertex agent policy head that cause mesh tangling are penalized (see Appendix E). At inference, we take the mode of this distribution, which is the direct output of the diffformer. The relocation map $\Phi^{(n)}$ thus inherits this non-tangling property, producing guaranteed valid meshes.

3.4 Reinforcement Learning Procedure and Mesh Update

In the following, we describe the data collection (rollout) process and the policy update step. The entire procedure for a single training step is illustrated in Figure 4. This diagram shows how the agent transitions the mesh from a state $\mathcal{T}^{(n)}$ to the next state $\mathcal{T}^{(n+1)}$ by applying the learned policy, and how the resulting information is used to update the network via PPO.

Rollout structure. Training data is collected by executing the policy in the simulation environment for trajectories of a fixed length N . A single trajectory consists of N sequential mesh adaptation steps. Within each trajectory, steps $n = 0, \dots, N - 2$ involve a full hr -adaptation (relocation followed by refinement). The final step, $n = N - 1$, performs only the relocation step.

One hr -adaptivity step. A single, complete adaptive step from mesh $\mathcal{T}^{(n)}$ to $\mathcal{T}^{(n+1)}$ unfolds as follows:

1. **State Construction:** Given the current mesh $\mathcal{T}^{(n)}$, the governing PDE is solved to obtain the discrete solution $u_{\mathcal{T}^{(n)}}$. From this solution, we compute per-vertex and per-element features (e.g., approximation errors, shape metrics), which are assembled into the hypergraph state representation $S^{(n)} = \mathcal{H}^{(n)}$.
2. **Network Forward Pass (Policies & Values):** The state $S^{(n)}$ is passed through the actor-critic network described in 3.3. The architecture produces four distinct outputs required for the PPO algorithm:
 - *Vertex Actor:* Parameters for a Gaussian distribution $\mathcal{N}(\boldsymbol{\mu}_i, \boldsymbol{\Sigma}_i)$ for every vertex \mathbf{z}_i .
 - *Element Actor:* A Bernoulli probability $p_j = \sigma(\ell_{K_j})$ for every element K_j .
 - *Critics:* Scalar value estimates $V_{\mathbf{z}_i}^{(n),r}$ and $V_{K_j}^{(n),h}$ estimating the expected return for vertex and element agents, respectively.
3. **Joint Action Sampling:** We sample the joint action $A^{(n)} = (A^{(n),r}, A^{(n),h})$ from the distributions parameterized in the previous step.
 - *Relocation Action:* New coordinates $\mathbf{z}'_i \sim \mathcal{N}(\boldsymbol{\mu}_i, \boldsymbol{\Sigma}_i)$ are sampled to form $A^{(n),r}$.
 - *Refinement Action:* Binary flags $a_{K_j} \sim \text{Bernoulli}(p_j)$ are sampled to form the refinement vector $\mathbf{b}^{(n)} = A^{(n),h}$.

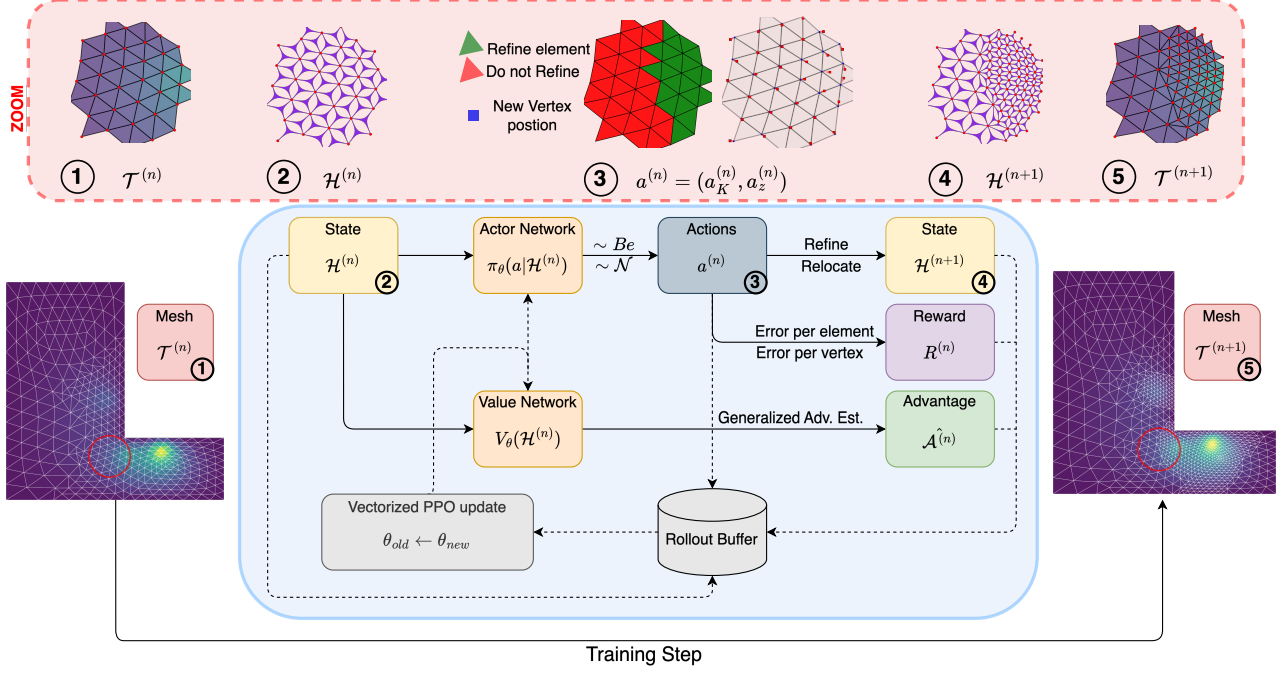


Figure 4: Overview of one HyperR training step, transitioning from mesh $\mathcal{T}^{(n)}$ (1) to $\mathcal{T}^{(n+1)}$ (5). The PPO loop (blue box) begins with the hypergraph state $\mathcal{H}^{(n)}$ (2), which is fed into the joint actor-critic network. The network outputs policy distributions and value estimates $V^{(n)}$. The policy π_θ samples a joint action $A^{(n)}$ (3), consisting of continuous vertex relocations ($\sim \mathcal{N}$) and binary element refinements ($\sim \text{Bernoulli}$). Applying these actions produces the intermediate relocated mesh $\tilde{\mathcal{T}}^{(n)}$ (4) and the final refined mesh $\mathcal{T}^{(n+1)}$ (5). Per-agent rewards $R^{(n)}$ are computed via FEM solves. The full transition tuple (state, action, reward, value) is stored in the rollout buffer. Once the trajectory is complete, GAE is applied retroactively to compute the advantages $\hat{\mathcal{A}}^{(n)}$ used for the vectorized PPO update (dashed line).

4. **Mesh Relocation & Intermediate Reward:** The relocation action $A^{(n),r}$ defines the map $\Phi^{(n)}$, transforming the current mesh into the intermediate mesh $\tilde{\mathcal{T}}^{(n)} = \mathcal{T}_{\Phi^{(n)}}$. As described in Sec. 3.3, boundary constraints are strictly enforced here. To compute the vertex rewards $r_{z_i}^{(n)}$, an intermediate FEM solve is performed on $\tilde{\mathcal{T}}^{(n)}$ to measure the immediate error reduction. (Note: This intermediate solve is strictly for training reward computation and is omitted during inference).
5. **Mesh Refinement & Final Reward:** The refinement vector $\mathbf{b}^{(n)}$ is applied to the moved mesh $\tilde{\mathcal{T}}^{(n)}$. We utilize standard conformity-preserving procedures—red-green-blue refinement in 2D Carstensen (2004)—to handle hanging nodes, producing the final mesh $\mathcal{T}^{(n+1)}$. A final FEM solve on $\mathcal{T}^{(n+1)}$ yields the element rewards $r_{K_j}^{(n)}$.
6. **Transition Storage:** The transition is completed by storing the tuple $(\mathcal{H}^{(n)}, A^{(n)}, R^{(n)}, V^{(n)}, \mathcal{H}^{(n+1)})$ in the rollout buffer. Advantage estimation is deferred until the full trajectory is collected; we then compute the advantages $\hat{\mathcal{A}}^{(n)}$ (which quantify how much better a specific action was compared to the state’s expected value) using Generalized Advantage Estimation (GAE) Schulman et al. (2016b) by processing the stored sequence of rewards and value estimates in reverse order.

Policy update. After collecting a batch of trajectories, the network parameters θ are updated. The goal of this update is to adjust the policy π_θ to maximize the expected future rewards (returns) collected by the agents. In RL, this is achieved by minimizing a specialized loss function (or “surrogate objective”) that is distinct from the error or cost functions defined in Section 2. We use the PPO algorithm Schulman et al. (2017), which defines a

composite loss $\mathcal{L}(\theta)$ designed to stably guide the policy toward higher rewards. As detailed in Appendix C.3, we optimize a loss function that addresses the multi-objective nature of the dual-swarm problem:

$$\mathcal{L}(\theta) = (L_r^\pi(\theta) + c_r L_r^V(\theta)) + (L_h^\pi(\theta) + c_h L_h^V(\theta)) - \alpha_{\text{ent}} H(\pi_\theta),$$

where L^π is the clipped surrogate policy loss and L^V is the clipped value function loss. The subscripts r and h denote the losses for the relocation (vertex) and refinement (element) agents, respectively. $H(\pi_\theta)$ is an entropy bonus to encourage exploration, and $(c_r, c_h, \alpha_{\text{ent}})$ are scalar weighting coefficients. The gradients of this combined loss are computed and used to update all shared and head-specific network parameters, thus completing one training iteration.

3.5 Reward Design and Training Curriculum

To guide the policy towards minimizing the global objective $\mathcal{J}(\Phi, \mathbf{b})$, defined in abstract form in equation (1), we design separate reward functions for the vertex and element agent swarms. In this respect, the minimization of the objective \mathcal{J} is actually performed by maximizing the expected total global return $J^{(0)} \approx J^{(0),r} + J^{(0),h}$ of the dual-swarm system. This total return decomposes into the aggregate contributions of the relocation and refinement swarms. These components are defined as the sum of discounted rewards over adaptation steps n : $J^{(0),r} = \sum_n \gamma_r^n \sum_{\mathbf{z}_i} r_{\mathbf{z}_i}^{(n),r}$ and $J^{(0),h} = \sum_n \gamma_h^n \sum_{K_j} r_{K_j}^{(n),h}$. Consequently, by designing the immediate rewards $r^{(n),\cdot}$ to scale with local error reduction, maximizing $J^{(0)}$ is equivalent to minimizing the cost functional \mathcal{J} .

To compute these rewards, we define two distinct error indicators for an element $K \in \mathcal{T}$ by projecting the high-fidelity solution from the reference mesh \mathcal{T}_{ref} . Let $P_K = \{p_{K^*} : K^* \in \mathcal{T}_{\text{ref}}, K^* \subset K\}$ be the set of centroids of reference elements contained within K . For refinement decisions, we employ the discrete L_∞ error $\eta_{K,\infty} = \max_{p \in P_K} |u_{\mathcal{T}}(p) - u_{\text{ref}}(p)|$, consistent with Freymuth et al. (2024b). For relocation and global monitoring, we utilize the discrete volume-weighted squared L_2 error, approximated as $\eta_{K,2}^2 = \sum_{p \in P_K} |K_p^*| |u_{\mathcal{T}}(p) - u_{\text{ref}}(p)|^2$, where $|K_p^*|$ is the volume of the reference element corresponding to centroid p .

These rewards serve as local proxies for error reduction and mesh quality. Moreover, we employ a two-phase training curriculum strategy: *Phase I* trains relocation with random refinement to learn stable geometry-aware features; *Phase II* jointly trains relocation and refinement to enable coordinated policies.

Per-vertex reward for relocation. The reward for a vertex agent is based on the immediate reduction in local error achieved through the relocation map $\Phi^{(n)}$. We first define a vertex-centric error for each $\mathbf{z}_i \in \mathcal{Z}^{(n)}$ as a volume-weighted average of the discrete squared L_2 error indicators $\eta_{K,2}^2$ of its incident elements denoted as $\{K \in E(\mathbf{z}_i)\}$:

$$\varepsilon_i^{(n)} = \frac{\sum_{K \in E(\mathbf{z}_i)} |K| \eta_{K,2}^2}{\sum_{K \in E(\mathbf{z}_i)} |K|}.$$

After applying the relocation to obtain the moved mesh $\tilde{\mathcal{T}}^{(n)}$, we recompute this error as $\varepsilon_i^{(n),+}$ and find the difference vector Δ with components $\Delta_i = \varepsilon_i^{(n)} - \varepsilon_i^{(n),+}$. Since the benefit of moving one vertex effects only its 1-hop neighborhood, we diffuse this raw signal across the vertex adjacency graph $A = A^{(n)}$ for 20 iterations of a Personalized PageRank update Gasteiger et al. (2019), with teleport probability $\beta = 0.5$, acting as a low pass filter:

$$\mathbf{r}^{\text{loc}} \leftarrow (1 - \beta) \Delta + \beta D^{-1} A \mathbf{r}^{\text{loc}}.$$

where D is the diagonal degree matrix. The final vertex reward vector $\mathbf{r}^{(n),r}$ is then obtained by normalizing this smoothed signal across the entire vertex set, i.e., $\mathbf{r}^{(n),r} = \mathbf{r}^{\text{loc}} / \|\mathbf{r}^{\text{loc}}\|_{l_\infty}$, to restrict values to $[-1, 1]$. Moreover, if any vertex movement results in a tangled element, the implicated vertices receive a strong penalty of -1.5 , while all others receive zero.

Per-element reward for refinement. The reward for an element agent, which guides the selection of the refinement vector $\mathbf{b}^{(n)}$, adapts the maximum-error-drop signal from ASMR⁺⁺ Freymuth et al. (2024b). The reward for refining the element K_j in the moved mesh $\tilde{\mathcal{T}}^{(n)}$ is:

$$r_{K_j}^{(n),h} = (\eta_{K_j,\infty} - \max_{k \in \text{children}(K_j)} \eta_{K_k,\infty}) - \alpha(|\text{children}(K_j)| - 1). \quad (2)$$

Here, $\text{children}(K_j)$ denotes the set of elements created when subdividing K_j by the chosen refinement procedure, and $|\text{children}(K_j)|$ is their count. The indicator $\eta_{\cdot,\infty}$ is normalized by the total initial error of the episode to ensure a consistent scale. The cost penalty coefficient α is drawn from a log-uniform distribution during training and supplied as a feature to the element agents, allowing the trained policy to adapt to different cost sensitivities at inference time without retraining.

Global reward components and returns. To prevent overly excessively local behavior and encourage globally beneficial adaptations, local agent returns are blended in a global signal. For an element agent acting on K_j , the final return is the average of its local return $J_{K_j}^{(n),h}$ and global return $J^{(n),h}$, which is the average of all element returns at that step:

$$\hat{J}_{K_j}^{(n),h} = \frac{1}{2} J_{K_j}^{(n),h} + \frac{1}{2} J^{(n),h}. \quad (3)$$

For vertex agents, the global signal $g^{(n)}$ is the fractional reduction of the total squared L_2 error across the mesh due to the relocation from $\mathcal{T}^{(n)}$ to $\tilde{\mathcal{T}}^{(n)}$:

$$g^{(n)} = \frac{\sum_{K \in \mathcal{T}^{(n)}} \eta_{K,2}^2 - \sum_{K \in \tilde{\mathcal{T}}^{(n)}} \eta_{K,2}^2}{\sum_{K \in \mathcal{T}^{(n)}} \eta_{K,2}^2}.$$

The final vertex return is then a blend of the local return $\hat{J}_{\mathbf{z}_i}^{(n),r}$ and $g^{(n)}$, and since they both roughly lie in $[-1, 1]$:

$$\hat{J}_{\mathbf{z}_i}^{(n),r} = \frac{1}{2} J_{\mathbf{z}_i}^{(n),r} + \frac{1}{2} g^{(n)}. \quad (4)$$

This was found to stabilize learning, as averaging the raw rewards directly proved too noisy.

Training curriculum. The learning problem is non-stationary: the refinement policy must act on a mesh that is being deformed by a relocation policy while it is being learned. To stabilize this co-adaptation, we employ a two-phase curriculum. In *Phase I*, the refinement actor-critic is frozen, and elements are split randomly. This allows the relocation policy to converge while being exposed to a wide variety of mesh topologies. In *Phase II*, the refinement policy is unfrozen, and both policies are trained jointly using the full Swarm-PPO update. This staged approach empirically removes learning oscillations and accelerates convergence to a robust, coordinated *hr*-policy.

4 Numerical Experiments and Results

In this section, we evaluate the proposed HypeR across four different 2D PDEs: the Poisson equation on L-shaped domains, the unsteady heat diffusion problem, where we consider the solution at the last time-instance of a preset trajectory, on square domains, Stokes flow on square domains with multiple rhomboid obstacles, and linear elasticity on L-shaped domains (detailed mathematical formulations of the PDE problems is provided in Appendix A). Figure 5 illustrates representative HypeR refinements for each equation, showcasing the method’s ability to adapt the mesh topology to the specific characteristics of different physical phenomena. The columns correspond to different values of the element-penalty characteristic, denoted as α and defined in equation (2), provided to the policy at inference. This value, which we vary to generate Pareto fronts, directly modulates the final mesh density (a lower penalty α corresponds to a denser mesh).

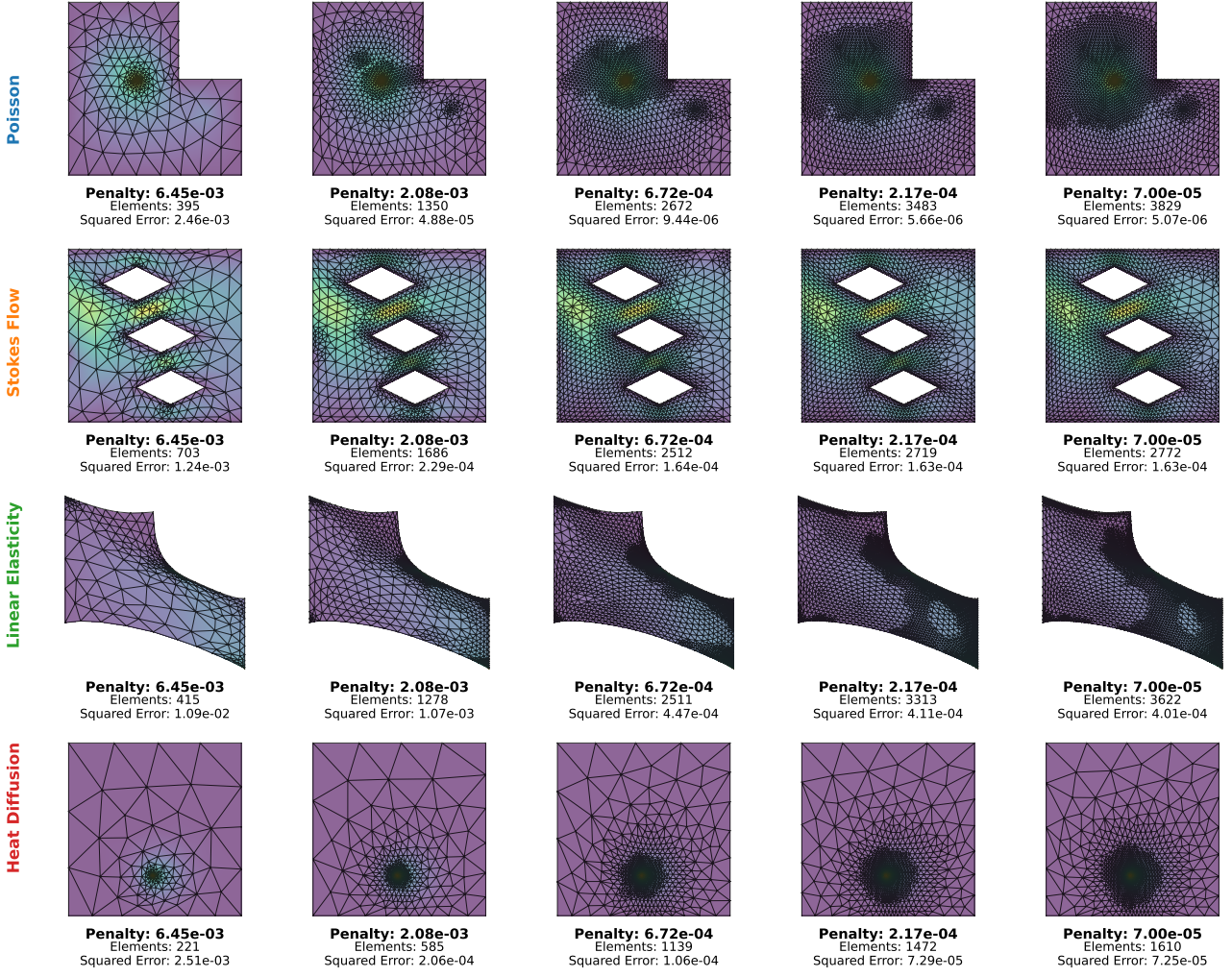


Figure 5: Representative HypeR refinements across four PDE problems (rows) for five penalty settings (columns). At inference time we set an element-penalty feature on hyperedges that controls the cost of adding elements; moving left to right the penalty decreases and the final mesh density increases. This single policy thus can be seen as producing a continuum of meshes by varying a single scalar input.

4.1 Experimental Setup

Our experimental protocol uses, at training time, a fixed dataset of 500 configurations, obtained by employing conforming triangular meshes with linear finite elements and varying the domain geometry and parameters (e.g., load positions and for Poisson/heat diffusion, inlet velocity profiles for Stokes, boundary conditions for the elasticity equation) for each PDE problem, each paired with corresponding initial and reference meshes. Initial meshes are deliberately coarse, containing 20-40 elements for most domains and 80-100 elements for Stokes flow due to the increased complexity of physical phenomenon. Reference meshes Ω_{ref} , on which the high-fidelity reference solutions are computed, are constructed by uniformly refining the initial mesh 6 times (5 times for Stokes flow due to computational constraints). These high-fidelity solutions are then used for reward computation, as in (3) and (4), during training.

Each refinement strategy operates for 4 adaptation steps across all equations except Stokes flow, which uses 3 steps. Within HypeR’s framework, this corresponds to 4 (or 3) combined relocation-refinement operations followed by a final relocation-only step that optimizes the final mesh node locations without adding elements. Training proceeds for 400 PPO iterations with a two-stage curriculum: during the first 150 iterations the relo-

cation policy is trained with frozen refinement (Phase I), followed by 250 iterations of joint training (Phase II) as described in Section 3.5.

We evaluate model performance using a discrete approximation of the element weighted L^2 -norm of the error computed on the reference mesh Ω_{ref} . Let \mathcal{T}_{ref} be its triangulation with elements K^* of volume $|K^*|$, and let \mathbf{u}_{ref} denote the FEM solution on \mathcal{T}_{ref} . For a solution $\mathbf{u}_{\mathcal{T}}$ obtained on a mesh \mathcal{T} , we evaluate it on the reference mesh via the interpolation operator Π_{ref} ⁴ and form the volume-weighted squared discrepancy:

$$\mathcal{E}^2(\mathcal{T}) = \sum_{K^* \in \mathcal{T}_{\text{ref}}} |K^*| \|\mathbf{u}_{\text{ref}}(p_{K^*}) - (\Pi_{\text{ref}}\mathbf{u}_{\mathcal{T}})(p_{K^*})\|_{\ell^2}^2,$$

where p_{K^*} is the centroid of the reference element K^* . We report the normalized squared error $\mathcal{E}_{\text{rel}}^2(\mathcal{T}) = \mathcal{E}^2(\mathcal{T})/\mathcal{E}^2(\mathcal{T}_{\text{init}})$ to enable comparison across PDEs. Model performance is assessed on a separate evaluation set of 100 PDE configurations. We evaluate each trained model across 20 different element penalty values α at inference time, producing a spectrum of mesh resolutions for comprehensive analysis. Complete hyperparameter specifications are provided in Appendix D. All experiments are repeated for 3 different random seeds.

4.2 Baselines and Comparisons

We compare HypeR against both learning-based and traditional adaptive mesh refinement methods. For learning-based comparisons, we evaluate our approach against ASMR++ Freymuth et al. (2024a), the current state-of-art deep RL approach for adaptive mesh refinement. ASMR++ employs a swarm-based multi-agent framework for h -adaptive refinement but lacks the r -adaptive vertex relocation capabilities of HypeR. We use identical experimental conditions for fair comparison: the same refinement steps, training and evaluation datasets, domain, and PDE formulations. We omit comparisons with other deep learning methods such as VDGNet Yang et al. (2023b), Single Agent Yang et al. (2023a), and Sweep Foucart et al. (2023), as ASMR++ has demonstrated superior performance against these baselines across similar problem settings.

For traditional heuristic methods, we compare HypeR against the maximum Error Oracle heuristic Dörfler (1996), which iteratively refines elements based on the maximum pointwise error within each element using oracle information from the reference mesh Ω_{ref} . We also evaluate the proposed approach against ZZ1 and ZZ2 error estimators, which employ the Zienkiewicz–Zhu Zienkiewicz and Zhu (1992) superconvergent patch recovery technique with 1 and 2 initial uniform refinement steps, respectively. The initial refinement steps are necessary as the ZZ error estimator produces unreliable results on very coarse meshes, failing to detect solution gradients in regions where elements are too large relative to the solution features.

All baseline methods operate under the same computational constraints and evaluation metrics as HypeR, enabling direct performance comparisons across the error-element count Pareto frontier.

4.3 Main Results

We evaluate HypeR along two dimensions: accuracy, or error reduction, and computational efficiency. For accuracy assessment, we employ Pareto curve plots showing the trade-off between element count and normalized squared error relative to the initial mesh. Each point represents the mean performance across our 100-evaluation dataset, with exponential saturation regression curves fitted to capture convergence behavior across the spectrum of mesh densities achieved by varying penalty parameters.

Accuracy analysis. Figure 6 demonstrates HypeR’s superior performance across all four benchmark problems. On the Poisson equation, HypeR achieves an error approximately 6 times smaller than ASMR++ at comparable element counts, while for linear elasticity, the error reduction reaches a factor of 10. The Stokes

⁴The operator Π_{ref} samples the continuous FEM function $u_{\mathcal{T}}$ at the centroids of the reference mesh elements. Specifically, for a centroid p_{K^*} of a reference element K^* , the value $(\Pi_{\text{ref}}u_{\mathcal{T}})(p_{K^*})$ is determined by identifying the coarse element $K \in \mathcal{T}$ such that $p_{K^*} \subset K$ and evaluating the solution using the basis functions associated to K in p_{K^*} points in space.

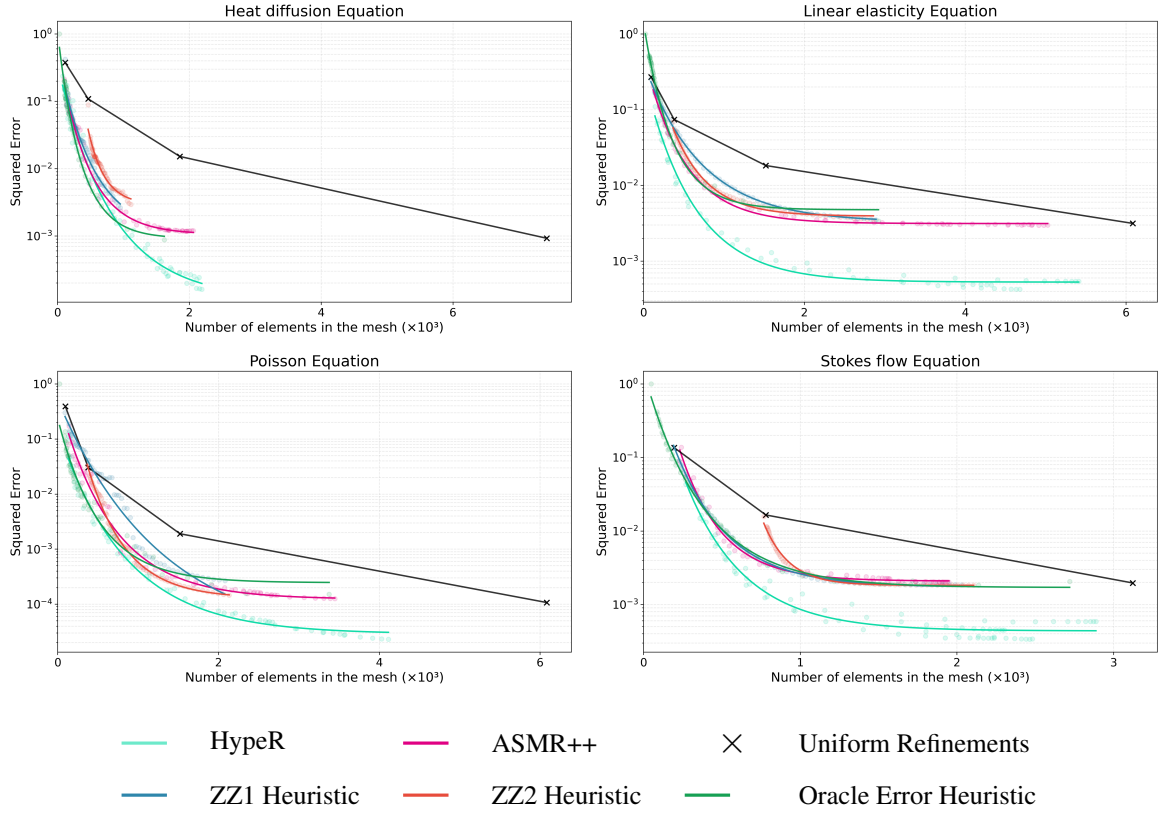


Figure 6: Convergence analysis across four benchmark PDEs showing squared error vs. number of mesh elements. HypeR (water green) consistently achieves lower error than ASMR++ (magenta), ZZ1/ZZ2 (blue/light red), Oracle (green), and uniform refinement (black crosses). Exponential saturation curves fitted to mean performance over 100 test instances.

flow and heat diffusion problems show consistent improvements, with errors from 3 to 5 times smaller, as HypeR maintains steeper error reduction over the evaluated element ranges with respect to the other methods which quickly attain an error plateau.

A critical insight emerges from the exponential saturation analysis: ASMR++, ZZ1, ZZ2, and Oracle approaches all converge to accuracy limits imposed by uniform mesh refinement constraints. These methods can only subdivide existing elements, creating an inherent ceiling around 10^{-3} to 10^{-4} normalized error, corresponding to the best accuracy achievable through only element subdivision. HypeR fundamentally overcomes this limitation through its joint relocation-refinement approach, achieving error levels of 10^{-4} to 10^{-5} while using $2 - 3\times$ fewer elements than uniform refinement. This joint capability allows HypeR to simultaneously modify the mesh topology (via subdivision) and optimize its geometry (via vertex relocation) to better align with solution features.

Computational efficiency and robustness To provide a direct statistical comparison complementary to the Pareto curves in Figure 6, Table 1 aggregates performance over specific intervals of element counts (e.g., 2500–3500 elements for Poisson). Since adaptive strategies dictate the final mesh size dynamically, they rarely produce meshes with identical element counts. Therefore, we define a representative target interval for each PDE and compute the mean error with standard deviation and runtime for all evaluation episodes where the final mesh size falls within this range. This binning approach allows us to compare several methods average performance under similar resolution constraints. Within these intervals, HypeR consistently achieves the lowest mean error, outperforming the strongest baseline (ASMR++) by factors ranging from $2.9\times$ (Poisson) to

over $6\times$ (linear elasticity). Regarding computational costs, while the joint *hr*-formulation introduces a modest overhead relative to ASMR++ ($1.5\text{--}2\times$ inference time) due to the additional relocation head and intermediate solver step, HypeR remains orders of magnitude faster than the Oracle heuristic and competitive with ZZ estimators. This confirms that the method delivers a superior trade-off, converting a small investment in inference compute into substantial gains in approximation accuracy.

PDE	Elements Range	Mean Time (s)					Mean Error				
		HypeR	ASMR++	Oracle	ZZ1	ZZ2	HypeR	ASMR++	Oracle	ZZ1	ZZ2
Poisson	2500-3500	0.209 ± 0.029	0.107 ± 0.017	2.462 ± 14.86	0.979 ± 5.41	1.036 ± 5.61	4.36e-5 $\pm 4.36e-5$	1.28e-4 $\pm 1.16e-4$	1.51e-4 $\pm 1.56e-4$	1.07e-4 $\pm 8.52e-5$	1.04e-4 $\pm 8.71e-5$
Stokes Flow	1000-2000	0.440 ± 0.076	0.274 ± 0.039	3.749 ± 17.93	1.887 ± 7.63	0.779 ± 3.88	8.34e-4 $\pm 5.35e-4$	2.32e-3 $\pm 9.80e-4$	2.02e-3 $\pm 6.43e-4$	1.97e-3 $\pm 6.57e-4$	2.01e-3 $\pm 6.98e-4$
Linear Elasticity	2000-5000	0.523 ± 0.120	0.312 ± 0.069	2.130 ± 10.78	0.530 ± 2.97	0.555 ± 2.99	4.95e-4 $\pm 4.09e-4$	3.16e-3 $\pm 1.08e-3$	3.53e-3 $\pm 8.55e-4$	3.41e-3 $\pm 1.03e-3$	3.35e-3 $\pm 1.00e-3$
Heat Diffusion	1300-2000	0.278 ± 0.039	0.167 ± 0.021	3.746 ± 12.32	0.699 ± 2.74	0.366 ± 0.77	3.61e-4 $\pm 5.62e-4$	1.32e-3 $\pm 1.61e-3$	1.06e-3 $\pm 9.85e-4$	1.45e-3 $\pm 1.91e-3$	1.52e-3 $\pm 2.19e-3$

Table 1: Performance comparison across four PDE benchmarks. HypeR achieves the lowest error (bold) across all problems while maintaining competitive computational times compared to traditional heuristic methods.

Generalization tests. Beyond in-distribution testing, we assess zero-shot generalization along two directions. First, we scale the Poisson problem from the unit square domain used during training to a much larger $\Omega = [6, 6]$ ($36\times$ larger area) and apply both HypeR and ASMR++ without any retraining. Figure 7 shows that HypeR maintains high mesh quality: elements remain well-shaped with smooth density transitions and align with level curves of the solution, concentrating resolution where gradients are highest. In contrast, ASMR++ produces significantly coarser meshes in critical regions, exhibits less smooth density transitions, and yields visibly higher local error in the zoomed panels where accuracy is most needed. These results indicate that HypeR’s joint relocation-refinement policy is robustly transferred to substantially larger domains.

Second, we evaluate cross-geometry generalization on an unseen ”bow-tie” domain with a narrow bottleneck in the center, shared across all equations. Figure 8 (grid across penalties) illustrates that HypeR adapts effectively to this out-of-distribution shape, producing meshes with the same desirable properties observed in-distribution: smooth gradation, alignment to solution anisotropy through relocation, and well-shaped elements without tangling. Performance trends remain consistent across PDEs and penalty settings, demonstrating that the learned policy is not specialized to the training domains.

Reference mesh speedup. The computational benefits become most evident when comparing HypeR against the cost of obtaining the high-fidelity reference solution. We define the speedup as the ratio between the runtime of solving the PDE on the reference mesh Ω_{ref} , constructed by performing $N + 1$ uniform subdivisions of the initial domain, where N is the maximum refinement depth of the HypeR policy, and the total runtime entailed by the HypeR framework (comprising neural network inference, mesh updates, and the final FEM solve). As shown in Figure 9, HypeR achieves speedups ranging from $4\times$ to over $100\times$. This advantage is particularly pronounced for complex physics like Stokes flow and linear elasticity, where the use of FEM makes the brute-force uniform refinement of Ω_{ref} prohibitively expensive compared to the targeted allocation of degrees of freedom by HypeR.

Qualitative mesh analysis. Beyond quantitative performance metrics, HypeR produces meshes with demonstrably superior geometric properties compared to refinement-only approaches. Figure 10 illustrates this through a detailed comparison on the Poisson equation, where HypeR generates meshes with smoother transitions in element size, aspect ratio, and skewness as they approach regions of high solution curvature. While ASMR++ exhibits abrupt dimensional changes due to hard refinement constraints, HypeR’s continuous relocation capability

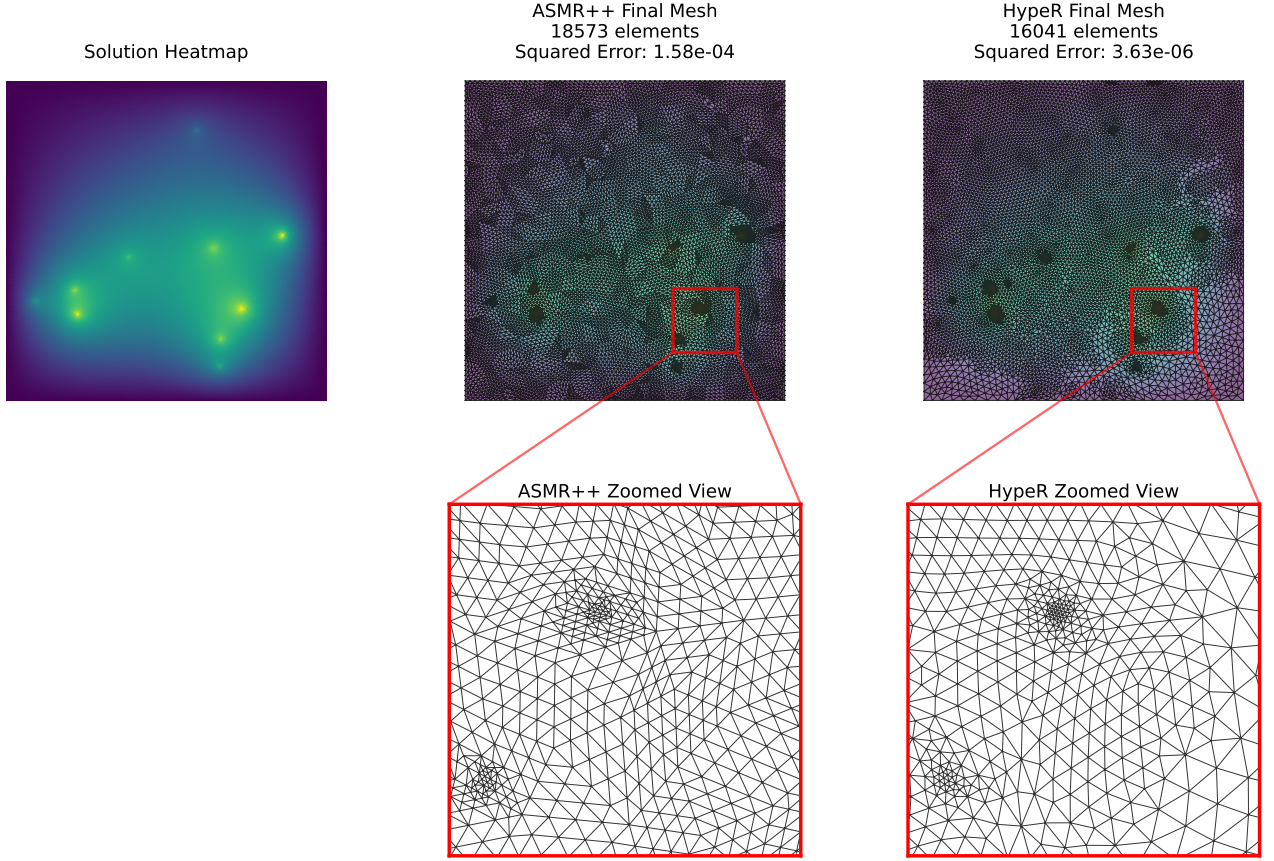


Figure 7: Generalization to much larger domains for Poisson equation (the domain is a 6×6 square versus 1×1 in training). Top: solution field with final mesh overlays for HypeR and ASMR++; bottom: matched zooms. HypeR preserves alignment with solution level sets and smooth mesh gradation, while ASMR++ remains coarser and less smooth in density transitions, leading to higher local error precisely where increased resolution is needed.

enables gradual mesh density variations that better follow the underlying solution structure. The topology generated by HypeR shows improved alignment with the solution’s contour regions, creating element boundaries that naturally follow level curves of the physical field. This geometric coherence translates directly into computational efficiency: well-aligned meshes reduce numerical diffusion, improve condition number of the resulting linear system, and enable more accurate gradient computations with fewer DOFs. The smooth element-size grading also mitigates issues commonly associated with abrupt refinement interfaces - i.e., sharp element-size jumps across neighboring cells - which tend to introduce poorly shaped elements (e.g., extreme aspect ratios, small angles, or high skewness) and numerical artifacts at refinement interfaces. These qualitative improvements complement the quantitative accuracy gains, demonstrating that HypeR’s joint optimization approach produces not merely smaller errors, but fundamentally better-structured computational domains. The resulting meshes exhibit the hallmarks of expert-designed adaptations, that is smooth density transitions, solution-aligned topology, and optimal element quality distributions, achieved automatically through the learned policy. These geometric improvements validate our core hypothesis that joint *hr*-optimization fundamentally outperforms sequential approaches, not just in numerical metrics but in producing meshes that better capture the underlying physics.

Algorithmic evolution. To further illustrate the mechanisms behind HypeR’s quantitative gains, Figure 11 compares the step-by-step adaptation of HypeR and ASMR++ on the Stokes flow problem. For HypeR (top

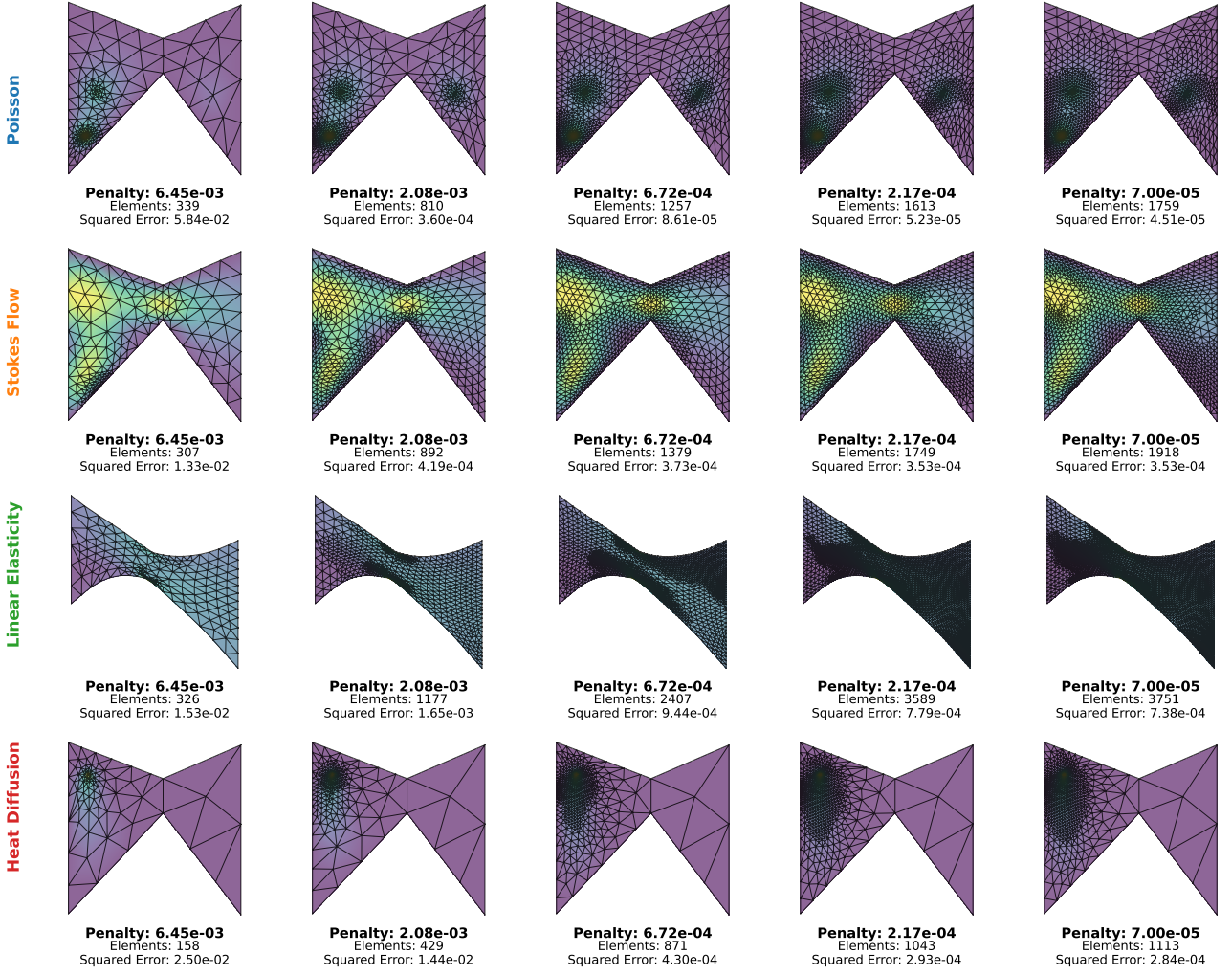


Figure 8: Generalization to different domain shape (unseen during training): a bow-tie geometry with a narrow bottleneck shared across all PDEs. Final meshes and solutions across penalty settings are shown. Hyper retains smooth density transitions, solution-aligned anisotropy, and well-shaped elements without tangling across PDE equations, indicating robust cross-geometry transfer.

row), relocation and refinement are jointly executed at each iteration, followed by a final relocation-only step. This coordination yields substantial error reduction at every stage: relocation alone decreases error significantly before refinement even occurs, and the combined updates lead to a final mesh with evident lower error at a comparable number of elements. By contrast, ASMR++ (bottom row) performs only refinement steps, which steadily reduce error but cannot exploit vertex movement to precondition the mesh geometry. The annotated plots beneath each mesh report element counts, relative errors, and cumulative vertex displacement, quantifying how relocation accelerates convergence. This visualization highlights the qualitative difference between the two algorithms: Hyper actively reshapes the mesh to align with solution features, while ASMR++ relies solely on subdivision.

5 Conclusions and future work

This work introduces Hyper, the first deep RL framework that jointly learns mesh relocation and refinement policies through a unified neural architecture. By computing both continuous vertex displacements and discrete

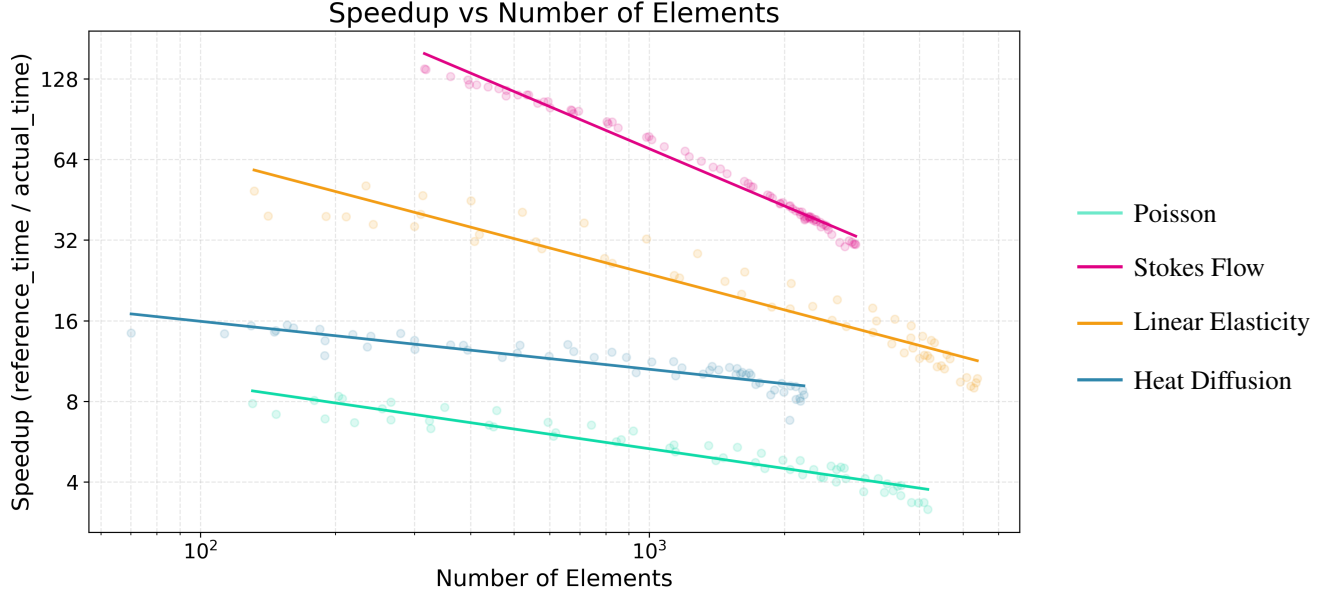


Figure 9: Speedup relative to computing the reference solution. We report the speedup $= T_{\text{solve}}(\Omega_{\text{ref}})/T_{\text{solve}}(\Omega_{\text{Hyper}})$ as a function of the final element count of the Hyper mesh. Each point represents the mean speedup over 100 problem’s configurations for a specific mesh density (controlled by the penalty α), demonstrating that Hyper is orders of magnitude faster than obtaining the equivalent ground-truth solution via uniform refinement.

refinement decisions in a single forward pass, Hyper discovers coordinated *hr*-adaptive strategies that fundamentally overcome the limitations of existing approaches. Our framework naturally encompasses pure *h*- and *r*-adaptivity as special cases (one needs to only disable the corresponding policy head), while its joint formulation enables synergies that cannot be achieved by sequential methods. The key insight is that the uniform refinement accuracy ceiling can be overcome through learned coordination between topology and geometric modifications.

Our hypergraph neural architecture enables this breakthrough by facilitating bidirectional information flow: element agents communicate refinement demands to vertex agents, which position themselves in advance to ensure well-conditioned subdivisions, while geometric distortion signals from vertex agents trigger targeted topological updates. This coordination, learned through our heterogeneous multi-agent formulation, with distinct discount factors capturing the different temporal impacts of relocation versus refinement, produces meshes achieving a 6–10 \times error decrease over state-of-art *h*-adaptive methods, while preserving computational efficiency with respect to both classical heuristics and uniform refinement.

Despite requiring complete FEM solves at each adaptation step and computationally intensive training, due to repeated error computations against reference solutions, Hyper opens promising avenues for accelerating scientific computing workflows. Extension to time-dependent PDEs, while requiring coarsening operations and projection maps for reward assignment on evolving topologies, appears tractable within our framework. Current works explore warm-start techniques and local solve strategies to reduce inference costs, while integration with surrogate models could yield accurate but extremely efficient solution approximations. More broadly, this work demonstrates that many numerical methods addressing *hr*-adaptivity meshing problems through staged procedures may benefit from joint learning approaches that discover coordination strategies beyond human heuristics. As the first method to break the uniform refinement barrier through learned *hr* coordination, Hyper establishes joint reinforcement-learned adaptivity as a powerful paradigm for automated mesh generation.

Acknowledgments

The authors wish to thank Christopher Irwin for the insightful discussions and valuable suggestions which contributed to the conceptual development of this work. We also thank Niklas Freymuth and his collaborators for their work on ASMR++, and for making their implementation publicly available; their open-source code provided an invaluable foundation for this project.

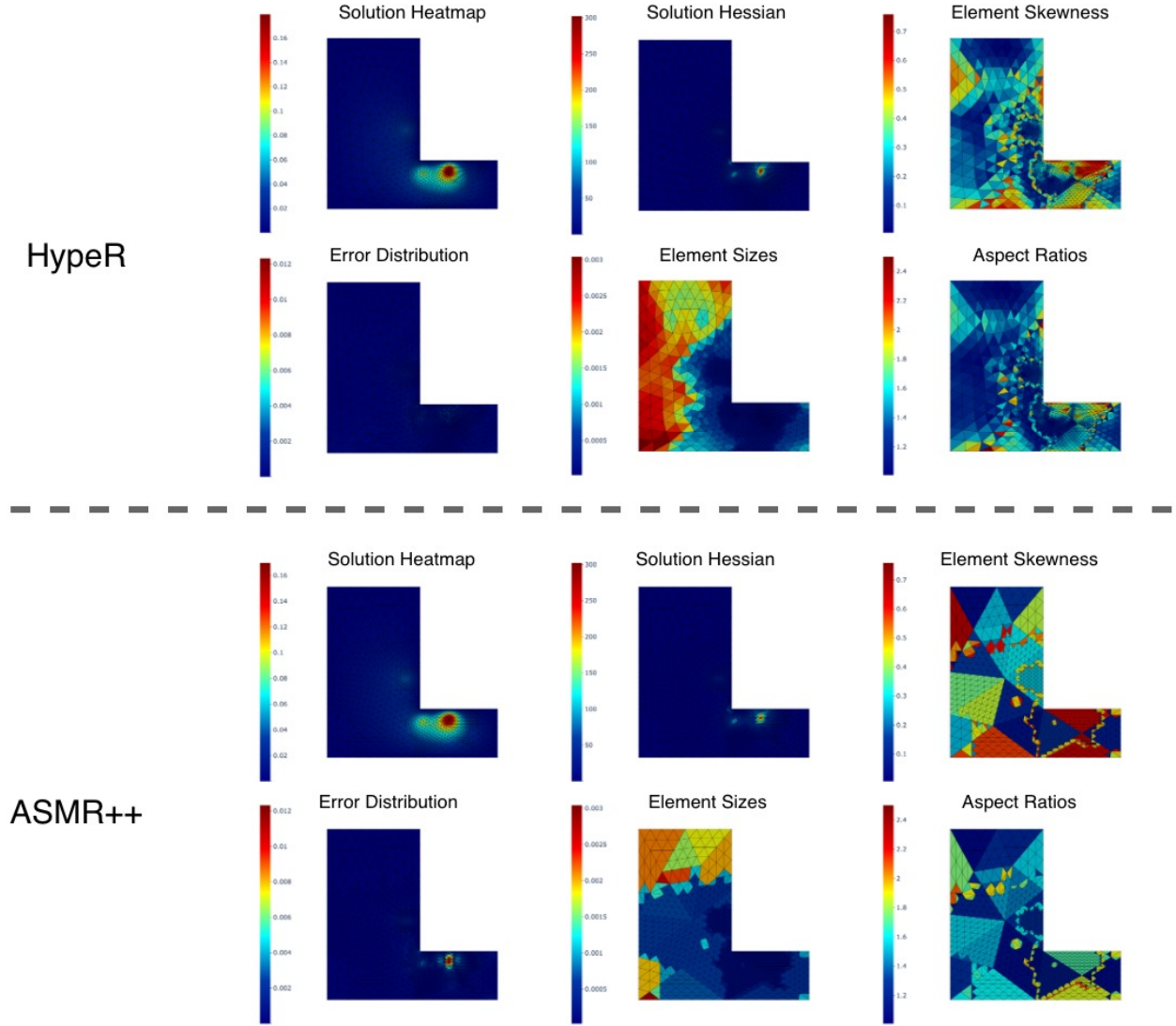


Figure 10: Comparison of mesh quality metrics between ASMR++ (bottom) and HypeR (top) tested on the Poisson equation. HypeR demonstrates superior performance highlighted by smoother transitions in both aspect ratio and skewness across elements, while ASMR++ exhibits abrupt changes and regional concentrations of these properties. HypeR’s element size gradually decreases in regions of high solution curvature, in contrast to ASMR++’s abrupt dimensional changes due to hard refinement constraints. Additionally, HypeR’s mesh exhibits improved alignment with the solution’s contour regions.

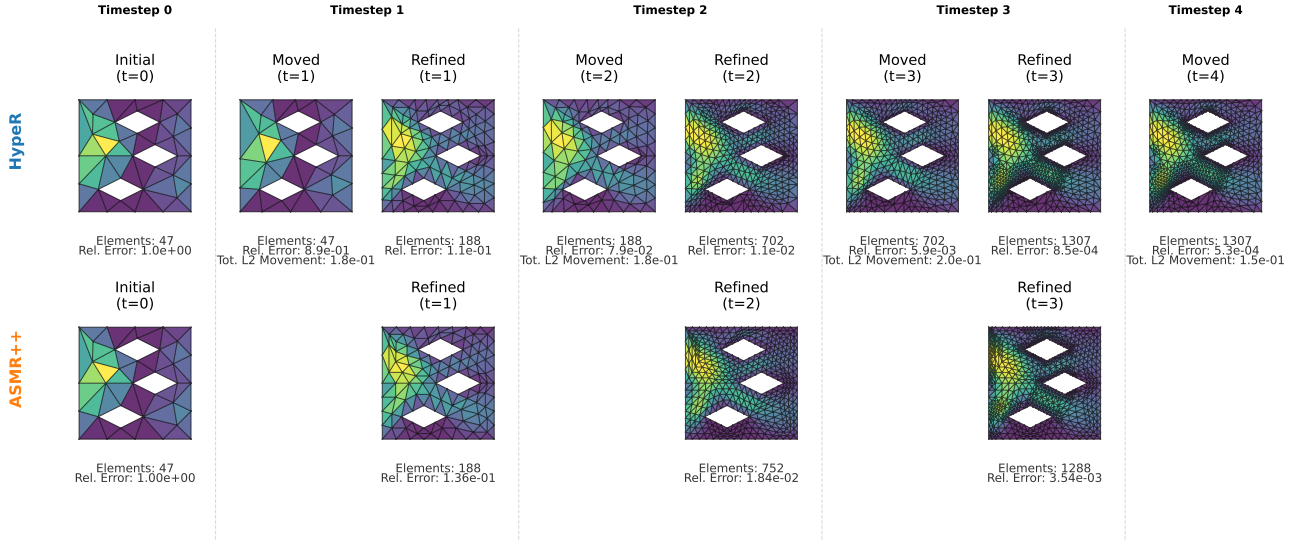


Figure 11: Step-by-step mesh evolution for HypeR (top row) and ASMR++ (bottom row) on a representative Stokes flow problem. Each panel shows the mesh at an adaptation iteration along with corresponding element counts, relative L^2 error as defined in the Experimental Setup, and (for HypeR) total vertex displacement. HypeR’s relocation steps produce significant error reduction even before refinement, yielding a final mesh with substantially lower error at comparable resolution. ASMR++ reduces error only through refinement, without geometric optimization.

References

- Mark Ainsworth and J Tinsley Oden. *A posteriori error estimation in finite element analysis*. John Wiley & Sons, 2000.
- Frédéric Alauzet and Adrien Loseille. A decade of progress on anisotropic mesh adaptation for computational fluid dynamics. *Computer-Aided Design*, 72:13–39, 2016.
- Ivo Babuška and Manil Suri. The p and h-p versions of the finite element method, basic principles and properties. *SIAM review*, 36(4):578–632, 1994.
- Randolph E Bank and Jinchao Xu. Some refinement algorithms and data structures for regular local mesh refinement. *Scientific Computing: Applications of Mathematics and Computing to the Physical Sciences*, pages 3–17, 2003.
- Peter Binev, Wolfgang Dahmen, and Ron DeVore. Adaptive finite element methods with convergence rates. *Numerische Mathematik*, 97:219–268, 2004.
- Jan Bohn and Michael Feischl. Recurrent neural networks as optimal mesh refinement strategies. *Computers & Mathematics with Applications*, 97:61–76, 2021.
- Yann Brenier. Polar factorization and monotone rearrangement of vector-valued functions. *Communications on Pure and Applied Mathematics*, 44(4):375–417, 1991. doi: 10.1002/cpa.3160440402.
- Susanne C Brenner and L Ridgway Scott. *The mathematical theory of finite element methods*. Springer, 2008.
- Chris J Budd, Weizhang Huang, and Robert D Russell. Adaptivity with moving grids. *Acta Numerica*, 18: 111–241, 2009.
- Carsten Carstensen. Adaptive finite element methods and a posteriori error estimation: An overview of theory and algorithms. *Numerical Methods for Partial Differential Equations*, 2004. Overview including conformity-preserving red–green/blue refinement strategies in 2D.
- Gian Luca Delzanno, Luis Chacón, John M Finn, Y Chung, and Giovanni Lapenta. An optimal robust equidistribution method for two-dimensional grid adaptation based on monge–kantorovich optimization. *Journal of Computational Physics*, 227(23):9841–9864, 2008.
- Willy Dörfler. A convergent adaptive algorithm for poisson’s equation. *SIAM Journal on Numerical Analysis*, 33(3):1106–1124, 1996.
- Tarik Dzanic, Ketan Mittal, Dohyun Kim, Jiachen Yang, Socratis Petrides, Brendan Keith, and Robert Anderson. Dynamo: Dynamic anticipatory mesh optimization for multi-agent reinforcement learning on time-dependent pdes. *Journal of Computational Physics*, 506, 2024.
- Alexandre Ern and Jean-Luc Guermond. *Theory and practice of finite elements*. Springer, 2004.
- Lawrence C Evans. *Partial differential equations*. American Mathematical Society, 2010.
- Yifan Feng, Haoxuan You, Zizhao Zhang, Rongrong Ji, and Yue Gao. Hypergraph neural networks. In *Proceedings of the AAAI Conference on Artificial Intelligence*, volume 33, pages 3558–3565, 2019.
- Corbin Foucart, Aaron Charous, and Pierre FJ Lermusiaux. Deep reinforcement learning for adaptive mesh refinement. *Journal of Computational Physics*, 491:112381, 2023.

- Niklas Freymuth, Philipp Dahlinger, Tobias Würth, Simon Reisch, Luise Kärger, and Gerhard Neumann. Swarm reinforcement learning for adaptive mesh refinement. In *Advances in Neural Information Processing Systems (NeurIPS)*, volume 36, 2023.
- Niklas Freymuth, Philipp Dahlinger, Tobias Würth, Simon Reisch, Luise Kärger, and Gerhard Neumann. Adaptive swarm mesh refinement using deep reinforcement learning with local rewards. *Journal of Machine Learning Research*, 2024a.
- Niklas Freymuth, Philipp Dahlinger, Tobias Würth, Simon Reisch, Luise Kärger, and Gerhard Neumann. Adaptive swarm mesh refinement using deep reinforcement learning with local rewards. *Journal of Machine Learning Research (under review)*, 2024b. arXiv:2406.08440.
- Niklas Freymuth, Tobias Würth, Nicolas Schreiber, et al. Amber: Adaptive meshing by expert reconstruction. *arXiv preprint arXiv:2505.23663*, 2025. Under review.
- Johannes Gasteiger, Stefan Weißenberger, and Stephan Günnemann. Diffusion improves graph learning. In *Advances in Neural Information Processing Systems (NeurIPS)*, pages 13354–13366, 2019.
- Peiyan Hu, Yue Wang, and Zhi-Ming Ma. Better neural pde solvers through data-free mesh movers. In *The Twelfth International Conference on Learning Representations (ICLR)*, 2024.
- Keefe Huang, Moritz Krügener, Alistair Brown, Friedrich Menhorn, Hans-Joachim Bungartz, and Dirk Hartmann. Machine learning-based optimal mesh generation in computational fluid dynamics. *arXiv preprint arXiv:2102.12923*, 2021.
- Weizhang Huang and Robert D Russell. *Adaptive moving mesh methods*. Springer, 2011.
- Maximilian Hüttenrauch, Adrian Šošić, and Gerhard Neumann. Deep reinforcement learning for swarm systems. *Journal of Machine Learning Research*, 20(54):1–31, 2019.
- Volker John. *Finite Element Methods for Incompressible Flow Problems*, volume 51 of *Springer Series in Computational Mathematics*. Springer, Cham, Switzerland, 2016. ISBN 978-3-319-45750-5. doi: 10.1007/978-3-319-45750-5.
- Ainulla Khan, Moyuru Yamada, Abhishek Chikane, and Manohar Kaul. Graphmesh: Geometrically generalized mesh refinement using gnns. In *International Conference on Computational Science*, pages 120–134, 2024.
- Minseong Kim, Jaeseung Lee, and Jibum Kim. Gmr-net: Gcn-based mesh refinement framework for elliptic pde problems. *Engineering with Computers*, 39:3721–3737, 2023.
- Diederik P Kingma and Jimmy Ba. Adam: A method for stochastic optimization. *arXiv preprint arXiv:1412.6980*, 2014.
- Thomas N Kipf and Max Welling. Semi-supervised classification with graph convolutional networks. In *International Conference on Learning Representations (ICLR)*, 2017.
- Randall J LeVeque. *Finite difference methods for ordinary and partial differential equations*. SIAM, 2007.
- Andrew TT McRae, Colin J Cotter, and Chris J Budd. Optimal-transport-based mesh adaptivity on the plane and sphere using finite elements. *SIAM Journal on Scientific Computing*, 40(2):A1121–A1148, 2018.
- Ajay Nagarajan and Soheil Soghrati. Conforming to interface structured adaptive mesh refinement: 3d algorithm and implementation. *Computational Mechanics*, 62:1213–1238, 2018.

- Alfio Quarteroni, Riccardo Sacco, and Fausto Saleri. *Numerical Mathematics*, volume 37 of *Texts in Applied Mathematics*. Springer, Berlin, Heidelberg, 2nd edition, 2009. ISBN 978-3-540-34658-6. doi: 10.1007/978-0-387-22750-4.
- James Rowbottom, Georg Maierhofer, Teo Deveney, et al. G-adaptivity: Optimised graph-based mesh relocation for finite element methods. In *Proceedings of the International Conference on Machine Learning (ICML)*, 2025. Spotlight.
- Yousef Saad. *Iterative methods for sparse linear systems*. SIAM, 2003.
- John Schulman, Philipp Moritz, Sergey Levine, Michael Jordan, and Pieter Abbeel. High-dimensional continuous control using generalized advantage estimation. In *International Conference on Learning Representations*, 2016a.
- John Schulman, Philipp Moritz, Sergey Levine, Michael Jordan, and Pieter Abbeel. High-dimensional continuous control using generalized advantage estimation. In *Proceedings of the International Conference on Learning Representations (ICLR)*, 2016b.
- John Schulman, Filip Wolski, Prafulla Dhariwal, Alec Radford, and Oleg Klimov. Proximal policy optimization algorithms. In *arXiv preprint arXiv:1707.06347*, 2017. URL <https://arxiv.org/abs/1707.06347>.
- Wenbin Song, Mingrui Zhang, Joseph G Wallwork, et al. M2n: Mesh movement networks for pde solvers. In *Advances in Neural Information Processing Systems (NeurIPS)*, volume 35, pages 7199–7210, 2022.
- Adrian Šošić, Wasiur R KhudaBukhsh, Abdelhak M Zoubir, and Heinz Koepl. Inverse reinforcement learning in swarm systems. In *Proceedings of the 16th Conference on Autonomous Agents and MultiAgent Systems*, pages 1413–1421, 2017.
- Rob Stevenson. The completion of locally refined simplicial partitions created by bisection. *Mathematics of Computation*, 77(261):227–241, 2008.
- Richard S Sutton and Andrew G Barto. *Reinforcement learning: An introduction*. MIT press, 2018.
- Petar Veličković, Guillem Cucurull, Arantxa Casanova, Adriana Romero, Pietro Liò, and Yoshua Bengio. Graph attention networks. In *International Conference on Learning Representations (ICLR)*, 2018.
- Rüdiger Verfürth. *A Review of A Posteriori Error Estimation and Adaptive Mesh-Refinement Techniques*. Wiley-Teubner Series Advances in Numerical Mathematics. Wiley, Chichester, 1996. ISBN 0-471-96795-5.
- Zhichao Wang et al. Ugm2n: Unsupervised generalizable mesh movement network. *arXiv preprint arXiv:2408.08615*, 2024.
- Naganand Yadati, Madhav Nimishakavi, Prateek Yadav, Venkata Subrahmanyam Nitin, Partha Talukdar, and Massimiliano Melucci. Hypergc: A new method of training graph convolutional networks on hypergraphs. In *Advances in Neural Information Processing Systems (NeurIPS)*, 2019.
- Jiachen Yang, Tarik Dzanic, Brenden K Petersen, Jun Kudo, Ketan Mittal, Vladimir Tomov, Jean-Sylvain Camier, Tuo Zhao, Hongyuan Zha, Tzanio Kolev, Robert Anderson, and Daniel Faissol. Reinforcement learning for adaptive mesh refinement. In *Proceedings of the International Conference on Artificial Intelligence and Statistics (AISTATS)*, 2023a.
- Jiachen Yang, Ketan Mittal, Tarik Dzanic, Socratis Petrides, Brendan Keith, Brenden Petersen, Daniel Faissol, and Robert Anderson. Multi-agent reinforcement learning for adaptive mesh refinement. In *Proceedings of the International Conference on Autonomous Agents and Multiagent Systems (AAMAS)*, 2023b.

- Masayuki Yano and David L Darmofal. An optimization-based framework for anisotropic simplex mesh adaptation. *Journal of Computational Physics*, 231(22):7626–7649, 2012.
- Jian Yu, Hongqiang Lyu, Ran Xu, Wenxuan Ouyang, and Xuejun Liu. Flow2mesh: A flow-guided data-driven mesh adaptation framework. *Physics of Fluids*, 36(3), 2024.
- Jian Yu, Hongqiang Lyu, Xuejun Liu, et al. Para2mesh: A dual diffusion framework for moving mesh adaptation. *Chinese Journal of Aeronautics*, 2025.
- Mingrui Zhang, Chunyang Wang, Stephan Kramer, Joseph G Wallwork, et al. Um2n: Universal mesh movement networks. In *Advances in Neural Information Processing Systems (NeurIPS)*, 2024. Spotlight.
- Zheyang Zhang, Yongxing Wang, Peter K Jimack, and He Wang. Meshingnet: A new mesh generation method based on deep learning. In *International Conference on Computational Science*, pages 186–198, 2020.
- Zheyang Zhang, Peter K Jimack, and He Wang. Meshingnet3d: Efficient generation of adapted tetrahedral meshes for computational mechanics. *Advances in Engineering Software*, 157–158:103021, 2021.
- Olgierd Cecil Zienkiewicz and Jian Zhong Zhu. The superconvergent patch recovery and a posteriori error estimates. part 1: The recovery technique. *International Journal for Numerical Methods in Engineering*, 33(7):1331–1364, 1992.

A Systems of Equations

The following briefly describes the system of equations used for our experiments, including the PDE problem, domains, and process conditions. Each task uses an underlying system of equations and varies either the process conditions, the used domain, or both. For some tasks, we add additional information about the task as node features to the observation graph of the GNN policy.

A.1 Poisson’s Equation

We address Poisson’s Equation

$$-\Delta u(\mathbf{x}) = f(\mathbf{x}) \quad \text{in } \Omega,$$

where $f(\mathbf{x})$ is the load function. The solution $u(\mathbf{x})$ must satisfy the Dirichlet boundary condition $u(\mathbf{x}) = 0$ on $\partial\Omega$. We use an L-shaped domain Ω , defined as $(0, 1)^2 \setminus (p_0 \times (1, 1))$, where the lower left corner p_0 is sampled from $U(0.2, 0.95)$ in x and y direction.

We employ a Gaussian Mixture Model with three components for each problem’s load function. The mean of each component is drawn from $U(0.1, 0.9)^2$, with rejection sampling ensuring all means reside within Ω . We then independently draw diagonal covariances from a log-uniform distribution $\exp(U(\log(0.0001, 0.001)))$ and randomly rotate them to yield a full covariance matrix. Component weights are generated from $\exp(N(0, 1)) + 1$ and subsequently normalized. The load function evaluation at each face’s midpoint is used as a node feature.

A.2 Stokes Flow

Let $\mathbf{u}(\mathbf{x})$ and $p(\mathbf{x})$ represent the velocity and pressure fields, respectively, in a channel flow. We analyze the Stokes flow without a forcing term. The strong form of the problem reads:

$$\begin{cases} -\nu\Delta\mathbf{u} + \nabla p = \mathbf{0} & \text{in } \Omega, \\ \nabla \cdot \mathbf{u} = 0 & \text{in } \Omega, \end{cases}$$

where ν represents the kinematic viscosity (Quarteroni et al., 2009). The velocity field at the inlet is defined as

$$\mathbf{u}(x=0, y) = \begin{pmatrix} u_p y(1-y) + \sin(\varphi + 2\pi y) \\ 0 \end{pmatrix}.$$

At the outlet, we impose the condition $\nabla\mathbf{u}(x=1, y) = \mathbf{0}$, and assume a no-slip condition $\mathbf{u} = \mathbf{0}$ at all other boundaries. For numerical stability, we utilize P_1/P_2 Taylor-Hood elements, with quadratic velocity and linear pressure shape functions (John, 2016).

The inlet profile parameter u_p is sampled from a log-uniform distribution $\exp(U(\log(0.5, 2)))$. The domain is structured as a unit square with three rhomboid holes of length 0.4 and height 0.2. The holes are centered at $y \in \{0.2, 0.5, 0.8\}$ and we randomly sample their x-coordinate from $U(0.3, 0.7)$. We optimize the meshes w.r.t. the velocity vector and present a scalar error as the norm of the vectorized velocity error.

A.3 Linear Elasticity

We investigate the steady-state deformation of a solid under stress caused by displacements at the boundary $\partial\Omega$ of the domain Ω . Let $\mathbf{u}(\mathbf{x})$ be the displacement field. The equilibrium equation is given by

$$-\nabla \cdot \boldsymbol{\sigma}(\mathbf{u}) = \mathbf{0} \quad \text{in } \Omega,$$

where $\boldsymbol{\sigma}$ is the linear-elastic and isotropic stress tensor defined as

$$\boldsymbol{\sigma}(\mathbf{u}) = 2\mu\boldsymbol{\varepsilon}(\mathbf{u}) + \lambda\text{tr}(\boldsymbol{\varepsilon}(\mathbf{u}))\mathbf{I}.$$

Here, $\varepsilon(\mathbf{u}) = \frac{1}{2}(\nabla \mathbf{u} + (\nabla \mathbf{u})^\top)$ is the infinitesimal strain tensor. The Lamé parameters are derived from Young’s modulus $E = 1$ and Poisson ratio $\nu = 0.3$:

$$\lambda = \frac{E\nu}{(1+\nu)(1-2\nu)} \quad \text{and} \quad \mu = \frac{E}{2(1+\nu)}.$$

We use the same class of L-shaped domains as in the Poisson problem in Section A.1. We fix the displacement of the left boundary to 0, i.e., $\mathbf{u}(x = 0, y) = \mathbf{0}$, and randomly sample a displacement direction from $U[0, \pi]$ and magnitude from $U(0.2, 0.8)$ to displace the right boundary as $\mathbf{u}(x = 1, y) = \mathbf{u}_P$. The stress $\boldsymbol{\sigma} \cdot \mathbf{n} = \mathbf{0}$ is zero normal to the boundary at both the top and bottom of the part (traction-free condition). The task-dependent displacement vector \mathbf{u}_P is added as a globally shared node feature to all elements. Our objective includes the norm of the displacement field \mathbf{u} and the resulting Von-Mises stress, using an equal weighting between the two.

A.4 Non-Stationary Heat Diffusion

Using temperature $u(\mathbf{x}, t)$ and a thermal diffusivity constant $a = 0.001$, we address a non-stationary thermal diffusion problem defined by

$$\frac{\partial u}{\partial t} - a\Delta u = f \quad \text{in } \Omega \times (0, T].$$

Here, $f(\mathbf{x}, \tau)$ is a position-dependent heat distribution

$$f(\mathbf{x}, \tau) = 1\,000 \exp(-100 \|\mathbf{x} - \mathbf{p}_\tau(\tau)\|_1),$$

where $\|\cdot\|_1$ denotes the L_1 norm. The position of the heat source’s path $\mathbf{p}_\tau(\tau) = (x_p(\tau), y_p(\tau))$ is linearly interpolated over time as

$$\mathbf{p}_\tau = \mathbf{p}_0 + \frac{\tau}{\tau_{\max}}(\mathbf{p}_{\tau_{\max}} - \mathbf{p}_0).$$

The start and goal positions \mathbf{p}_0 and $\mathbf{p}_{\tau_{\max}}$ are randomly drawn from the entire domain. The temperature u is set to zero on all boundaries $\partial\Omega$. We use a total of $\tau_{\max} = 20$ uniform time steps in $\{0.5, \dots, 10\}$ and an implicit Euler method for the time-integration. Domain geometry is derived from 10 equidistant points on a circle centered at $(0.5, 0.5)$ with a radius of 0.4. Each point is randomly distorted by a value $U(-0.2, 0.2)^2$ before we proceed to calculate the points convex hull as our domain. We finally normalize the convex hull to lie in $(0, 1)^2$. The result is a family of convex polygons with up to 10 vertices. We provide and measure the error and solution of the final simulation step, and provide the distance to the start and end position of the heat source as additional node features for each element.

B Mesh Feature Definitions and Metrics

We construct feature vectors for both vertices and elements to capture the geometric configuration, solution state, and topological constraints of the mesh.

B.1 Vertex Features

For every vertex $z_i \in \mathcal{Z}^{(n)}$ at iteration n , we construct a feature vector $f_{z_i}^{(n)} \in \mathbb{R}^{d_v}$ concatenating position, physical state, and boundary constraints:

$$f_{z_i}^{(n)} = \left[z_i^{(n)}, u_i^{(n)} \right]^\top.$$

Here, $z_i^{(n)} \in \mathbb{R}^d$ denotes the coordinate vector ($d \in \{2, 3\}$), which is the primary input for the Diffformer’s relocation predictions. The scalar $u_i^{(n)}$ represents the nodal FEM solution value.

B.2 Element Features

For each element $K_j \in \mathcal{T}^{(n)}$, we assemble a feature vector $f_{K_j}^{(n)} \in \mathbb{R}^{d_e}$ that aggregates geometric quality, local solution statistics, and task-specific parameters:

$$f_{K_j}^{(n)} = \left[|K_j|, \bar{u}_{K_j}, \sigma_{u,K_j}, n, \alpha_c, \mathbf{s}_{K_j}^\top, \mathbf{v}_{K_j}^\top \right]^\top.$$

The basic components include the element measure $|K_j|$ (area in 2D) and the first two statistical moments of the solution within the element: the mean \bar{u}_{K_j} and standard deviation σ_{u,K_j} , computed over the element’s vertex set $V(K_j)$. We also include the current adaptation step n and the cost penalty coefficient α_c . The latter is sampled from a log-uniform distribution during training to allow the network to learn a spectrum of density preferences, enabling adaptive control over the error-cost trade-off at inference time.

The remaining components, shape quality \mathbf{s}_{K_j} and solution variability \mathbf{v}_{K_j} , are defined below.

B.2.1 Element Shape Metrics (\mathbf{s}_{K_j})

The shape feature vector quantifies element distortion and orientation, differing by dimension.

2D Triangular Elements. We define $\mathbf{s}_{K_j} = [\rho_{K_j}, \sin \theta_{K_j}, \cos \theta_{K_j}]^\top$. The aspect ratio is given by $\rho_{K_j} = \ell_{\max}/\ell_{\min}$, the ratio of the longest to shortest edge lengths. The orientation is derived from the principal stretch direction of the element. Let $J_{K_j} \in \mathbb{R}^{2 \times 2}$ be the Jacobian matrix defined by the edge vectors incident to a reference vertex. We perform a Singular Value Decomposition (SVD) $J_{K_j} = U\Sigma V^\top$ and extract the angle of the principal axis as $\theta_{K_j} = \arctan 2(U_{1,0}, U_{0,0})$.

B.2.2 Solution Variability Metrics (\mathbf{v}_{K_j})

To guide refinement in regions of high error, we compute a variability vector $\mathbf{v}_{K_j} = [\|\nabla u\|, g_{\max}, g_{\text{std}}, a_{\text{align}}]^\top$. The first component, $\|\nabla u\|$, represents the Euclidean norm of the constant solution gradient inherent to the linear finite element formulation. To capture solution fluctuations across element boundaries, we calculate the normalized solution jumps $|\Delta u_e/\ell_e|$ for every edge $e \in E(K_j)$, incorporating both their maximum, g_{\max} , and standard deviation, g_{std} , into the feature vector. Finally, to detect anisotropic features, we compute a scalar alignment metric a_{align} between the solution gradient and the element’s principal stretch direction \mathbf{d}_{K_j} (derived from the orientation θ_{K_j} in 2D):

$$a_{\text{align}} = \frac{\nabla u \cdot \mathbf{d}_{K_j}}{\|\nabla u\| \|\mathbf{d}_{K_j}\|}.$$

C Background on Neural Networks and Reinforcement Learning

This appendix section establishes the core theoretical and architectural foundations necessary for the HypeR framework. We review the mathematical concepts of the Markov Decision Process (MDP), detail the specific challenges addressed by Swarm Reinforcement Learning, and derive the Hypergraph Neural Network architecture that provides the required permutation-invariant and dual-fidelity mesh representation.

C.1 Reinforcement Learning Foundations

Reinforcement Learning (RL) Sutton and Barto (2018) provides a mathematical framework for sequential decision-making under uncertainty, formalized as a Markov Decision Process (MDP). An MDP is characterized by the tuple $\langle \mathcal{S}, \mathcal{A}, P, R, \gamma \rangle$, comprising the state space \mathcal{S} , the action space \mathcal{A} , the transition dynamics $P : \mathcal{S} \times \mathcal{A} \times \mathcal{S} \rightarrow [0, 1]$, a scalar reward function $R : \mathcal{S} \times \mathcal{A} \rightarrow \mathbb{R}$, and a discount factor $\gamma \in [0, 1]$.

In this setting, an agent interacts with the environment by observing a state $s_t \in \mathcal{S}$ and sampling an action $a_t \sim \pi(\cdot|s_t)$ from its policy. This action triggers a transition to $s_{t+1} \sim P(\cdot|s_t, a_t)$ and yields a reward

$r_t = R(s_t, a_t)$. The agent’s goal is to optimize the policy parameters θ to maximize the expected cumulative discounted return $J(\pi) = \mathbb{E}_{\tau \sim \pi} [\sum_{t=0}^{\infty} \gamma^t r_t]$, where τ denotes the trajectory.

To estimate the quality of the policy, we employ standard value functions: the state-value function $V^\pi(s) = \mathbb{E}[G_t | s_t = s]$ and the action-value function $Q^\pi(s, a) = \mathbb{E}[G_t | s_t = s, a_t = a]$, where G_t is the return from time t . The difference between these, $A^\pi(s, a) = Q^\pi(s, a) - V^\pi(s)$, yields the Advantage function, which quantifies the relative benefit of a specific action over the average policy behavior. We optimize the policy directly via the Policy Gradient Theorem:

$$\nabla_{\theta} J(\pi_{\theta}) = \mathbb{E}_{\pi_{\theta}} [\nabla_{\theta} \log \pi_{\theta}(a_t | s_t) A^{\pi_{\theta}}(s_t, a_t)].$$

This formulation allows for the optimization of stochastic policies, a requirement for the continuous action spaces inherent to vertex relocation tasks.

C.2 Deep Reinforcement Learning for Swarm Systems

Swarm systems Hüttenrauch et al. (2019) consist of multiple homogeneous agents that must coordinate to achieve collective objectives. Each agent typically has limited individual capabilities, requiring emergent collective intelligence through local interactions. This setting presents fundamental challenges that distinguish it from both single-agent RL and general multi-agent RL.

C.2.1 Fundamental Challenges in Swarm RL

Scalability and Dimensionality: Traditional multi-agent RL approaches concatenate observations from all agents, creating state representations of size $O(N \cdot d_{obs})$ for N agents with d_{obs} -dimensional observations. For large swarms (e.g., meshes with thousands of elements), this leads to prohibitively high-dimensional input spaces that are computationally intractable for neural networks. Moreover, the policy network’s input layer must be sized for the maximum possible number of agents, wasting parameters when fewer agents are present.

Permutation Invariance: Swarm agents are inherently homogeneous and interchangeable—there is no fundamental difference between “agent 1” and “agent 2.” The optimal collective policy should be invariant to agent indexing: permuting agent labels should not change the behavior. However, standard neural networks treat input positions as distinct features, violating this symmetry and forcing the network to learn redundant mappings for all possible permutations.

Variable Population Sizes: Real swarm systems exhibit dynamic compositions where agents may be added, removed, or become temporarily unavailable (e.g., due to limited communication range). Neural network policies require fixed input dimensions, making them unsuitable for handling varying numbers of agents without architectural modifications or padding strategies that introduce bias.

Partial Observability and Local Interactions: In many swarm scenarios, agents have limited sensing capabilities and can only observe nearby neighbors within a communication or sensing radius. This creates a decentralized partially observable Markov decision process (Dec-POMDP) where each agent must make decisions based on incomplete local information. The observation set $O_i = \{o_{i,j} : j \in \mathcal{N}(i)\}$ for agent i contains only information about neighbors $\mathcal{N}(i)$, which may vary in size and composition over time.

Credit Assignment and Non-Stationarity: In cooperative swarms with shared rewards, determining which agents contributed to success or failure becomes challenging. Traditional swarm RL approaches typically provide the same global reward signal to all agents, making it difficult to attribute success or failure to individual agent actions. Additionally, from any individual agent’s perspective, the environment appears non-stationary as other agents’ policies evolve during training, violating the standard RL assumption of a fixed environment.

However, our mesh adaptation setting provides a significant advantage: we can compute dense, local reward signals specific to each agent based on local error reduction. For vertex agents, rewards are based on the immediate improvement in local discretization error achieved by their relocation. For element agents, rewards reflect the error reduction obtained through their refinement decisions. This dense reward structure substantially alleviates the credit assignment problem that typically plagues swarm RL systems.

C.2.2 Swarm MDP Formulation

Following the formalism of Hüttenrauch et al. (2019), we model the swarm as a specialized Decentralized Partially Observable MDP (Dec-POMDP). This construction proceeds by first defining an *agent prototype* $\mathcal{A} = \langle \mathcal{S}_{local}, \mathcal{O}, \mathcal{A}_{local}, \pi \rangle$, which encapsulates the capabilities of a single entity: its local state space \mathcal{S}_{local} , its observation space \mathcal{O} for perceiving neighbors, its available actions \mathcal{A}_{local} , and a shared decentralized policy $\pi : \mathcal{O} \times \mathcal{A}_{local} \rightarrow [0, 1]$.

The full Swarm MDP is then instantiated as the tuple $\langle N, \mathcal{A}, P, O, R \rangle$. Here, N represents the number of agents, which may vary over time. The global transition dynamics P and reward function R operate on the joint configuration of all N agents. Crucially, this formulation imposes *homogeneity*, meaning all agents share the same policy parameters, and *partial observability*, where the global state mapping $O : \mathcal{S}^N \times \{1, \dots, N\} \rightarrow \mathcal{O}$ restricts each agent’s view to its immediate topological neighborhood.

C.2.3 Application to Mesh Adaptation

We instantiate the Swarm MDP framework as a heterogeneous system comprising two distinct agent populations that cooperate to optimize the mesh.

Vertex Agents. Every vertex $z_i^{(n)}$ in the mesh functions as an independent agent tasked with minimizing local discretization error via geometric optimization. Its local state $s_{z_i} = [z_i^{(n)}, u_i^{(n)}]$ includes its spatial coordinates and solution value. Based on observations of its topological neighbors (incident elements and connected vertices), the agent outputs a continuous vector $a_{z_i} \in \mathbb{R}^d$ representing the new vertex location, effectively smoothing the mesh and concentrating degrees of freedom in high-error regions.

Element Agents. Every finite element $K_j^{(n)}$ acts as a discrete decision-maker responsible for topological refinement. Its state s_{K_j} aggregates geometric metrics (e.g., area, aspect ratio) and solution statistics (e.g., gradient variance). The agent selects a binary action $a_{K_j} \in \{0, 1\}$ determining whether to subdivide the element. This decision is driven by an objective to improve global approximation quality by increasing resolution in under-resolved areas.

Dynamic Composition. Unlike standard RL environments with fixed dimensions, the mesh adaptation process yields a complex adaptive system where the swarm composition evolves dynamically. A refinement action by an element agent spawns new vertex agents and increases the population of element agents for the subsequent timestep. Our use of a hypergraph neural network architecture is specifically designed to handle this variable cardinality, ensuring permutation-invariant processing of the growing agent population.

C.3 Proximal Policy Optimization for Swarm Systems

We employ Proximal Policy Optimization (PPO) Schulman et al. (2017) to optimize the policy parameters θ . PPO is particularly well-suited for our high-dimensional swarm action space due to its stability; it optimizes a clipped surrogate objective that prevents destructive policy updates by bounding the probability ratio $r_t(\theta) = \pi_\theta(a_t|s_t)/\pi_{\theta_{old}}(a_t|s_t)$ between the new and old policies.

C.3.1 Vectorized Swarm Formulation

Standard PPO implementations typically assume a single agent receiving a scalar reward. In our swarm setting, however, we must process the experiences of N concurrent agents, each receiving distinct, localized feedback. We therefore adopt a vectorized formulation where the rewards $\mathbf{r}_t \in \mathbb{R}^N$ and advantage estimates $\hat{\mathbf{A}}_t \in \mathbb{R}^N$ are treated as batch quantities. The swarm-averaged clipped loss is computed as:

$$L^{CLIP}(\theta) = \frac{1}{N} \sum_{i=1}^N \min \left(r_{t,i}(\theta) \hat{A}_{t,i}, \text{clip}(r_{t,i}(\theta), 1 - \epsilon, 1 + \epsilon) \hat{A}_{t,i} \right),$$

where indices i correspond to individual agents and ϵ is the clipping hyperparameter (set to 0.2). This vectorization is critical for the credit assignment problem in mesh adaptation: it ensures that a vertex agent moving effectively into a high-error region generates a strong positive gradient signal, even if a neighboring element agent performs a suboptimal refinement. By preserving the heterogeneity of the advantage vector $\hat{\mathbf{A}}_t$, the network can simultaneously reinforce successful local behaviors and suppress detrimental ones across the domain.

C.3.2 Heterogeneous Multi-Objective Optimization

The dual-swarm architecture of HypeR introduces a further complexity: vertex and element agents operate on distinct manifolds (continuous vs. discrete) with different reward scales and time horizons. To accommodate this, we construct a composite loss function that optimizes both populations simultaneously while allowing for distinct entropy regularization and value function scaling.

Let N_v and N_e denote the number of vertex and element agents at a given timestep. The total training objective $L(\theta)$ is defined as the weighted sum of the independent swarm losses:

$$\begin{aligned} L(\theta) = & \frac{1}{N_v} \sum_{i=1}^{N_v} (L_{v,i}^{CLIP}(\theta) + c_v L_{v,i}^{VF}(\theta) + \alpha_v H[\pi_{\theta,v}](s_{z_i})) \\ & + \frac{1}{N_e} \sum_{j=1}^{N_e} (L_{e,j}^{CLIP}(\theta) + c_e L_{e,j}^{VF}(\theta) + \alpha_e H[\pi_{\theta,e}](s_{K_j})). \end{aligned} \quad (5)$$

Here, L^{VF} represents the squared-error loss for the value function heads, and H denotes the entropy bonus used to encourage exploration. The coefficients c and α allow us to tune the learning dynamics for each agent type independently; for instance, we typically define distinct entropy coefficients α_v and α_e to balance the exploration rates of vertex relocation (continuous Gaussian exploration) versus element refinement (discrete Bernoulli exploration). This separation ensures that the shared hypergraph backbone learns representations that are robust for both geometric and topological decision-making.

C.4 Graph Neural Networks and Message Passing

Standard Convolutional Neural Networks (CNNs) rely on fixed grid structures and ordering, making them unsuitable for finite element meshes where connectivity is irregular and element indexing is arbitrary. Graph Neural Networks (GNNs) resolve this by operating on the graph topology $\mathcal{G} = (\mathcal{V}, \mathcal{E})$ directly. In the context of our Swarm RL formulation, GNNs provide the critical architectural inductive bias required to solve the challenges of scalability and permutation invariance outlined in Section C.

C.4.1 Message Passing and Swarm Invariance

The core mechanism of a GNN is *message passing*, where each vertex v_i updates its hidden state $\mathbf{h}_i^{(l)}$ by aggregating information from its local neighborhood $\mathcal{N}(i)$. This process is formalized as:

$$\mathbf{m}_i^{(l+1)} = \text{AGGREGATE}^{(l)} \left(\left\{ \mathbf{h}_j^{(l)} : j \in \mathcal{N}(i) \right\} \right), \quad (6)$$

$$\mathbf{h}_i^{(l+1)} = \text{UPDATE}^{(l)} \left(\mathbf{h}_i^{(l)}, \mathbf{m}_i^{(l+1)} \right). \quad (7)$$

This formulation directly satisfies the **Permutation Invariance** requirement of swarm systems. Because the aggregation function (e.g., sum, mean, max) is symmetric with respect to the input set $\{\mathbf{h}_j\}$, the output is independent of neighbor ordering. Consequently, permuting the indices of the mesh vertices results in a corresponding permutation of the output features: $\text{GNN}(\mathbf{P}\mathbf{X}) = \mathbf{P} \cdot \text{GNN}(\mathbf{X})$.

This property ensures that our agent policies are *universal*: the learned policy depends only on the local topological structure and features, not on the arbitrary global ID of the agent. This allows the same network weights to control a swarm of 100 agents or 10,000 agents without modification.

C.4.2 Attention Mechanisms

While basic GNNs (like GCNs Kipf and Welling (2017)) treat all neighbors equally during aggregation, mesh adaptation tasks often require focusing on specific regions of high error or geometric distortion. To enable this, we leverage mechanisms from Graph Attention Networks (GATs) Veličković et al. (2018).

Attention introduces learnable weights α_{ij} to the aggregation step:

$$\mathbf{h}_i^{(l+1)} = \sigma \left(\sum_{j \in \mathcal{N}(i)} \alpha_{ij} \mathbf{W}^{(l)} \mathbf{h}_j^{(l)} \right).$$

The coefficients α_{ij} allow the network to dynamically prioritize signals from specific neighbors—for instance, a vertex agent can learn to pay more attention to a neighbor with a high error gradient than to one in a resolved region. This anisotropic aggregation is particularly fundamental to the *Diffformer* block used in our relocation policy, where attention weights dictate the diffusion coefficients that drive vertex movement.

C.5 Hypergraph Neural Networks

Standard graph neural networks (GNNs) typically rely on pairwise message passing along edges, which is insufficient for capturing the volumetric constraints of finite element meshes. An element K_j —whether a triangle or tetrahedron—is defined by a set of vertices that collectively determine physical properties such as volume, aspect ratio, and Jacobian determinants. Decomposing these volumetric relationships into simple pairwise cliques inevitably leads to a loss of topological fidelity. To capture the full structural context required for mesh adaptation, we therefore adopt Hypergraph Neural Networks (HGNNs) (Feng et al., 2019). By operating directly on hyperedges that connect arbitrary subsets of vertices, HGNNs naturally model the element-vertex incidence structure without artificial reduction.

C.5.1 Hypergraph Mathematical Foundations

We formalize the mesh as a hypergraph $\mathcal{H} = (\mathcal{V}, \mathcal{E})$, comprising N vertices \mathcal{V} and M hyperedges (elements) \mathcal{E} . The connectivity is encoded by the incidence matrix $\mathbf{H} \in \{0, 1\}^{N \times M}$, where $H_{ij} = 1$ if vertex v_i belongs to hyperedge e_j . To normalize signal propagation across irregular meshes—where the number of elements meeting at a vertex (valence) varies significantly—we define the vertex degree matrix \mathbf{D}_v and hyperedge degree

matrix \mathbf{D}_e as diagonal matrices:

$$\mathbf{D}_v = \text{diag} \left(\sum_{j=1}^M H_{ij} \right), \quad \mathbf{D}_e = \text{diag} \left(\sum_{i=1}^N H_{ij} \right).$$

This formulation generalizes the standard adjacency matrix, allowing us to perform spectral convolutions on sets of arbitrary cardinality.

C.5.2 Dual Embedding Hypergraph Convolution

Standard HGCN architectures typically treat hyperedges as static connectors, using the incidence matrix merely to propagate information between vertices (effectively $\mathbf{H}\mathbf{H}^T$). This approach is insufficient for our multi-agent framework, where elements are active agents requiring their own latent representations to compute refinement values.

We therefore introduce a **Dual Embedding** architecture that maintains distinct, evolving latent states for both vertices, $\mathbf{X}^{(l)} \in \mathbb{R}^{N \times F}$, and hyperedges, $\mathbf{E}^{(l)} \in \mathbb{R}^{M \times F}$. The update rule $\Phi^{(l)} : (\mathbf{X}^{(l)}, \mathbf{E}^{(l)}) \rightarrow (\mathbf{X}^{(l+1)}, \mathbf{E}^{(l+1)})$ proceeds through a bidirectional message passing cycle consisting of three distinct phases:

1. Vertex-to-Hyperedge Aggregation. First, elements update their state by aggregating information from their constituent vertices. This step captures the geometric configuration of the element (e.g., distortion or tangle) derived from the current vertex positions. We employ a degree-normalized convolution:

$$\mathbf{Z}_\mathcal{E} = \sigma \left(\mathbf{D}_e^{-1} \mathbf{H}^T \mathbf{X}^{(l)} \mathbf{W}_{\mathcal{V} \rightarrow \mathcal{E}}^{(l)} \right),$$

where $\mathbf{W}_{\mathcal{V} \rightarrow \mathcal{E}}^{(l)}$ is a learnable weight matrix and σ is a non-linear activation (ReLU).

2. Hyperedge Feature Integration. To incorporate physics-aware data that exists strictly at the element level (such as error estimator values \mathbf{E}_{attr}), we fuse the aggregated geometric features $\mathbf{Z}_\mathcal{E}$ with the element’s intrinsic attributes. This fusion is performed via concatenation and a learned projection \mathbf{W}_{pool} :

$$\tilde{\mathbf{E}}^{(l+1)} = \mathbf{W}_{\text{pool}}^{(l)} \left[\mathbf{Z}_\mathcal{E} \parallel \mathbf{E}_{\text{attr}}^{(l)} \right].$$

This intermediate representation $\tilde{\mathbf{E}}^{(l+1)}$ serves as the updated state for the element agents.

3. Hyperedge-to-Vertex Aggregation. Finally, vertices update their representations by aggregating the enhanced features of the hyperedges they belong to. This step distributes global signals—such as high error flags or refinement needs—down to the local vertices to guide the relocation policy:

$$\mathbf{X}^{(l+1)} = \sigma \left(\mathbf{D}_v^{-1} \mathbf{H} \tilde{\mathbf{E}}^{(l+1)} \mathbf{W}_{\mathcal{E} \rightarrow \mathcal{V}}^{(l)} \right).$$

C.5.3 Architectural Advantages for Mesh Adaptation

This specific formulation offers critical advantages over standard GNNs. First, the bidirectional information flow ensures that vertex relocation is error-aware (receiving gradients from elements) and element refinement is geometry-aware (sensing distortion from vertices). Second, the separation of embedding spaces creates a natural multi-agent architecture, where the final representations $\mathbf{X}^{(L)}$ and $\mathbf{E}^{(L)}$ can be fed directly into separate actor-critic heads for vertex and element agents, respectively. Finally, the explicit degree normalization ensures scalability, allowing the policy to generalize zero-shot to meshes with vastly different resolutions and element counts.

D Hyperparameters

PPO Parameters We employ Proximal Policy Optimization with a training schedule of 400 iterations. Each iteration collects 256 environment transitions, which are subsequently used for 5 training epochs with mini-batches of size 32. The value function loss coefficient is set to 0.5, and we apply gradient norm clipping with a maximum norm of 0.5. Both policy and value function updates use a clip range of 0.2 to ensure stable learning. Observations are normalized using running estimates of mean and standard deviation. We configure agent-specific discount factors: $\gamma = 1.0$ for element agents to capture long-term refinement consequences, and $\gamma = 0.1$ for vertex agents to emphasize immediate relocation benefits. Advantage estimation follows the Generalized Advantage Estimation framework (Schulman et al., 2016a) with $\lambda = 0.95$. Individual agent advantages are computed by subtracting agent-specific value estimates from the combined local and global returns detailed in Section 3. These training parameters are identical to those used for ASMR++ to ensure fair comparison with the baseline method.

Neural Network Parameters The shared hypergraph convolutional backbone consists of 4 message passing layers, with separate parameter sets for element and vertex agents to prevent interference between their distinct learning objectives. We employ mean aggregation as the scatter-reduce operation for all hypergraph convolutions. The Diffformer block is configured with 4 learnable attention steps, where each step incorporates 2 diffusivity iterations (repeated applications with shared parameters) following the G-Adaptivity formulation (Rowbottom et al., 2025). The temporal discretization step size is set to $\delta\tau = 0.1$ to ensure mesh validity guarantees. All multi-layer perceptrons (MLPs) described in Section 3, including the policy and value heads, consist of 3 fully connected layers with tanh activation functions. We optimize all network parameters using the ADAM optimizer (Kingma and Ba, 2014) with a learning rate of 3.0×10^{-4} and no learning rate scheduling. For the ASMR++ baseline, we use the identical network architecture and hyperparameters as reported in their original work (Freymuth et al., 2024a).

Refinement Parameters All adaptive mesh refinement methods require control parameters to regulate the desired refinement level of the final mesh. Both HypeR and ASMR++ employ an element penalty parameter α that balances the cost of adding new elements against the benefit of refinement. Following the ASMR++ methodology, both methods are trained on a range of α values and condition their policies on this parameter, enabling adaptive mesh resolution during inference. For evaluation, we sample 20 penalty values log-uniformly distributed over the training ranges to produce meshes with varying element densities. The traditional heuristic methods (Oracle, ZZ1, ZZ2) refine elements based on estimated error indicators using an error threshold parameter θ that specifies which elements to refine based on the ratio between their local error and the maximum element error in the mesh. For these methods, we sample 100 values of θ uniformly distributed over their respective ranges. Table 2 summarizes the parameter ranges used for all methods across the four benchmark PDEs.

Table 2: Refinement parameter ranges for all methods across benchmark PDEs.

PDE	HypeR α	ASMR++ α	Oracle θ	ZZ1/ZZ2 θ
Poisson	$[7.0 \times 10^{-5}, 2.0 \times 10^{-2}]$	$[7.5 \times 10^{-3}, 2.0 \times 10^{-2}]$	$[0, 1]$	$[1.0 \times 10^{-4}, 1]$
Stokes Flow	$[7.0 \times 10^{-5}, 2.0 \times 10^{-2}]$	$[7.5 \times 10^{-3}, 2.0 \times 10^{-2}]$	$[0, 1]$	$[1.0 \times 10^{-4}, 1]$
Linear Elasticity	$[7.0 \times 10^{-5}, 2.0 \times 10^{-2}]$	$[7.5 \times 10^{-3}, 2.0 \times 10^{-2}]$	$[0, 1]$	$[1.0 \times 10^{-4}, 1]$
Heat Diffusion	$[7.0 \times 10^{-5}, 2.0 \times 10^{-2}]$	$[7.5 \times 10^{-3}, 2.0 \times 10^{-2}]$	$[0, 1]$	$[1.0 \times 10^{-4}, 1]$

These parameter ranges ensure comprehensive evaluation across the spectrum of mesh densities while maintaining fair comparison conditions between all methods.

E Implementation Details

In this section we detail the mechanisms for ensuring geometric validity during stochastic exploration, the strict enforcement of boundary conditions via coordinate transformations, and the mathematical properties of the differentiable relocation operator.

E.1 Mesh Tangling Detection and Penalization

A critical failure mode in learning-based mesh adaptation is mesh tangling, where vertex displacements cause elements to invert or overlap. Geometrically, this corresponds to a violation of the injectivity of the mapping from the reference element \hat{K} to the physical element $K_j^{(n)}$.

We define the validity of a mesh configuration $\mathcal{T}^{(n)}$ through the Jacobian of the affine transformation $F_K : \hat{K} \rightarrow K_j^{(n)}$. Let $J_{F_K}(\hat{\xi})$ denote the Jacobian matrix at reference coordinates $\hat{\xi}$. A strictly positive Jacobian determinant is required to preserve orientation:

$$\det(J_{F_K}(\hat{\xi})) > 0 \quad \forall \hat{\xi} \in \hat{K}.$$

In our experiments, we utilize linear simplicial elements (triangles in 2D). A property of these elements is that the Jacobian is constant over the domain \hat{K} , reducing the validity check to a single algebraic evaluation per element. For a 2D triangular element $K_j^{(n)}$ with vertices $\{z_{i_0}^{(n)}, z_{i_1}^{(n)}, z_{i_2}^{(n)}\}$, the Jacobian determinant can be computed as:

$$\det(J_{K_j^{(n)}}) = \det \begin{bmatrix} z_{i_1}^{(n)} - z_{i_0}^{(n)} \\ z_{i_2}^{(n)} - z_{i_0}^{(n)} \end{bmatrix}$$

Numerical Consequences. Tangling is not merely a geometric artifact but a catastrophic failure mode for the finite element method. Geometrically, an inverted element implies a negative measure (area or volume), which invalidates the change-of-variables formula used during the numerical integration of the weak form. Algebraically, this degeneracy manifests in the element stiffness matrix. As the Jacobian determinant approaches zero, the element quality degrades, causing the condition number of the system to explode. Once the element inverts ($\det(J) < 0$), the stiffness matrix loses its positive-definiteness. Consequently, the global linear system $\mathbf{K}\mathbf{u} = \mathbf{f}$ becomes ill-posed, typically causing iterative solvers (like Conjugate Gradient) to diverge or direct solvers to crash, rendering error evaluation impossible.

E.1.1 Tangling Penalization and Recovery

While the diffusion-based parameterization of the relocation policy theoretically guarantees $\det(J_\Phi) > 0$, strict validity applies only to the deterministic mean μ_i output by the network. To enable exploration, PPO samples actions from a stochastic Gaussian policy $\pi_\theta^r(\cdot | H^{(n)}) = \mathcal{N}(\mu_i, \Sigma_i)$. Consequently, large sampled deviations—common during the high-entropy early training phases—may push vertices beyond the validity envelope, resulting in element inversion.

Since a tangled mesh renders the subsequent Finite Element analysis mathematically ill-posed, we cannot compute the standard error-based reward. Instead, we implement a *geometric rollback* and a targeted penalization scheme. This approach prioritizes precise credit assignment: rather than punishing the entire swarm for a local violation, we identify and penalize only the specific agents responsible for the inversion.

Formally, let $\mathcal{I}^{(n)} = \{K \in \mathcal{T}_{\Phi^{(n)}} : \det(J_K) \leq 0\}$ be the set of inverted elements. We construct the set of culpable vertices $\mathcal{V}_{\text{penalty}}^{(n)}$ as the union of all vertices incident to elements in $\mathcal{I}^{(n)}$:

$$\mathcal{V}_{\text{penalty}}^{(n)} = \bigcup_{K \in \mathcal{I}^{(n)}} V(K).$$

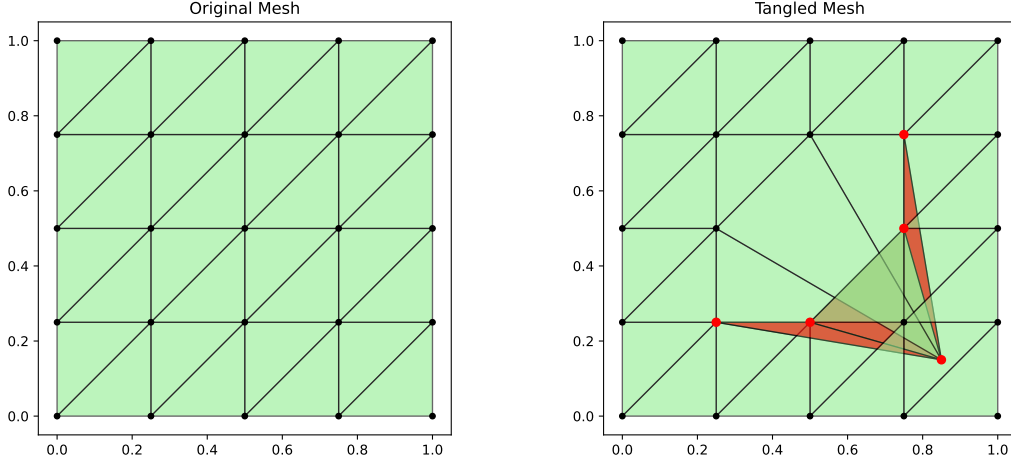


Figure 12: Illustration of the local penalization scheme. A purposefully displaced central vertex (right) causes geometric inversion in the adjacent elements (red). The penalty signal $r = -1.3$ is assigned exclusively to the vertices defining these inverted elements, isolating the geometric violation to the responsible agents.

Vertices in this set receive a punitive reward $r_{z_i}^{\text{loc}} = -\beta$, while all other vertices receive zero. We set $\beta = 1.3$ to ensure the penalty magnitude exceeds the standard reward bound of $[-1, 1]$, providing a strong "hard constraint" signal to the policy.

Following penalization, the system executes a recovery routine to preserve training stability. The invalid relocation step is discarded ($Z^{(n)} \leftarrow Z^{(n-1)}$), and the simulation proceeds to the refinement phase using the valid geometry from the previous iteration. This mechanism, visualized in Figure 12, allows the agents to learn validity constraints from negative feedback without causing solver crashes or terminating the episode.

E.2 Boundary Movement Constraints

Preserving the domain geometry Ω is critical; unconstrained updates to vertices on $\partial\Omega$ would violate the domain definition and invalidate the physics. We enforce these constraints structurally within the Diffformer by restricting the connectivity graph used for diffusion.

E.2.1 Geometric Classification

We classify boundary vertices based on their spatial degrees of freedom. Corner vertices ($\mathcal{V}_{\text{corner}}$) are geometrically fixed ($d\mathbf{z}/dt = 0$). Edge vertices ($\mathcal{V}_{\text{edge}}$) are constrained to move along specific boundary lines. We denote the set of all boundary vertices belonging to a specific geometric component k (e.g., a specific edge or face) as $\mathcal{V}_{\partial}^{(k)}$.

E.2.2 Constraint Enforcement via Masked Diffusion

The Diffformer updates vertex positions via the graph diffusion ODE $\frac{d\mathbf{Z}}{d\tau} = (\mathbf{A}_{\theta} - \mathbf{I})\mathbf{Z}$. A fundamental property of this process is that it moves each vertex strictly into the convex hull of its neighbors defined by \mathbf{A}_{θ} .

Since the boundaries in our domains are linear (straight lines since we are in the 2D case), any convex combination of points lying on a boundary component will also lie on that component. Therefore, we can enforce constraints without explicit projection operators simply by masking the adjacency matrix. We construct a constrained adjacency $\tilde{\mathbf{A}}_{\theta}$ such that boundary vertices only attend to neighbors on the same component:

$$\tilde{A}_{ij} = \begin{cases} A_{ij} & \text{if } i \in \mathcal{V}_{\text{interior}} \\ A_{ij} & \text{if } i, j \in \mathcal{V}_{\partial}^{(k)} \text{ (same boundary component)} \\ 0 & \text{otherwise} \end{cases}$$

By zeroing out connections between the interior and the boundary, as well as connections between disjoint boundary components (e.g., two different edges), we ensure that the update for a boundary vertex remains strictly within its assigned geometry.

E.2.3 Boundary-Consistent Stochastic Policy

While the deterministic Diffformer output is guaranteed to respect boundary constraints via the masked adjacency matrix, the *stochastic* policy required for PPO exploration poses a challenge. Sampling a displacement vector \mathbf{a}_{z_i} from a generic Gaussian $\mathcal{N}(\boldsymbol{\mu}, \boldsymbol{\Sigma})$ in \mathbb{R}^d would almost certainly violate the boundary geometry (e.g., pushing an edge vertex off its line). Projecting the sampled action back onto the boundary is undesirable as it distorts the probability density function, invalidating the PPO likelihood ratio.

Instead, we parameterize the policy for boundary vertices directly within their permissible local coordinate systems. For each vertex $z_i \in \mathcal{V}_{\text{boundary}}$, we construct a local orthonormal basis \mathbf{B}_i aligned with the boundary geometry:

- Edge vertices: $\mathbf{B}_i = [\mathbf{t}_i] \in \mathbb{R}^{d \times 1}$, where \mathbf{t}_i is the unit tangent vector of the edge.
- Corner vertices: The basis is empty (0 degrees of freedom).

The policy network outputs distribution parameters for the coefficients $\boldsymbol{\alpha}$ in this reduced space, rather than the global coordinates. The reduced policy π_{red} and the subsequent reconstruction of the global action a_{z_i} are defined as:

$$a_{z_i} = \mathbf{B}_i \boldsymbol{\alpha}, \quad \text{where } \boldsymbol{\alpha} \sim \begin{cases} \mathcal{N}(\boldsymbol{\mu}_t, \boldsymbol{\Sigma}_t^2) & \text{if } z_i \in \mathcal{V}_{\text{edge}} \\ \mathcal{N}(\boldsymbol{\mu}_{uv}, \boldsymbol{\Sigma}_{uv}) & \text{if } z_i \in \mathcal{V}_{\text{face}} \\ \delta(\mathbf{z}_i) & \text{if } z_i \in \mathcal{V}_{\text{corner}} \end{cases}$$

For the PPO update, we compute the log-probability of an action strictly in the reduced space. Given a global displacement a_{z_i} , we recover the local coefficients via projection $\boldsymbol{\alpha} = \mathbf{B}_i^T a_{z_i}$. The log-likelihood is then:

$$\log \pi_{\theta}(a_{z_i} | s) \equiv \log \pi_{\text{red}}(\boldsymbol{\alpha} | s).$$

This formulation ensures that all exploration remains strictly geometrically valid while preserving differentiability and the correct normalization of the probability density.

E.3 Diffformer: Diffusion-Based Mesh Relocation Operator

The vertex relocation policy in HypeR is parameterized through a diffusion-based operator, termed the *diffformer*, which ensures provably valid mesh transformations while remaining fully differentiable. This operator, adapted from G-Adaptivity (Rowbottom et al., 2025), addresses the critical challenge of mesh tangling that commonly affects learning-based mesh relocation methods.

E.3.1 Mathematical Formulation

The diffformer recasts vertex relocation as a graph diffusion process over pseudo-time τ . Given the current vertex coordinates $Z^{(n)} = \{z_i^{(n)}\}_{i=1}^{N_v}$ at iteration n , the evolution follows the ordinary differential equation:

$$\frac{dZ(\tau)}{d\tau} = (A_{\theta}(X^k) - I)Z(\tau) = -\Delta_{\theta}Z(\tau)$$

where $Z(0) = Z^{(n)}$ and $\Delta_\theta = I - A_\theta(X^k)$ is a learnable, weighted graph Laplacian. The row-stochastic attention matrix $A_\theta(X^k)$ is computed dynamically from the vertex embeddings $\{h_i^{(L)}\}_{i=1}^{N_v}$ provided by the hypergraph backbone:

$$[A_\theta(X^k)]_{ij} = \frac{\exp(\phi_\theta(h_i^{(L)}, h_j^{(L)}))}{\sum_{k \in \mathcal{N}(i)} \exp(\phi_\theta(h_i^{(L)}, h_k^{(L)}))}$$

where ϕ_θ is a learnable attention function and $\mathcal{N}(i)$ denotes the neighborhood of vertex i in the mesh graph.

The diffusion equation is integrated over a fixed interval $[0, \tau_{end}]$ using forward Euler discretization with step size $\delta\tau$:

$$Z^{(m+1)} = Z^{(m)} + \delta\tau \cdot (A_\theta(X^k) - I)Z^{(m)} = (I + \delta\tau(A_\theta(X^k) - I))Z^{(m)}$$

for $m = 0, 1, \dots, \lfloor \tau_{end}/\delta\tau \rfloor$. The final vertex positions $Z(\tau_{end})$ serve as the mean μ for the Gaussian vertex policy $\pi_\theta^r(a_{z_i}|H^n) = \mathcal{N}(\mu_i, \Sigma_i)$.

E.3.2 Intuition and Design Principles

The diffformer leverages the fundamental property that diffusion processes move each vertex toward a weighted convex combination of its neighbors' positions. This geometric constraint ensures that:

1. Locality preservation: Vertices move smoothly within the convex hull of their neighborhood
2. Adaptive anisotropy: The learned attention weights A_θ allow for direction-dependent diffusion that adapts to solution features
3. Topological invariance: The mesh connectivity remains unchanged while optimizing vertex positions

Unlike classical velocity-based mesh movement methods that can produce arbitrary displacements leading to element inversion, the diffusion formulation inherently constrains the solution space to geometrically valid configurations, i.e. reserves element orientations, ensuring no mesh tangling occurs.